Space Weather

RESEARCH ARTICLE
10.1029/2018SW001999

Modeling Geoelectric Fields in Ireland and the UK for Space Weather Applications

J. Campanyà[1,2], P. T. Gallagher[1,2], S. P. Blake[1,3,4], M. Gibbs[5], D. Jackson[5], C. D. Beggan[6], G. S. Richardson[6], and C. Hogg[2]

[1]School of Physics, Trinity College Dublin, Dublin, Ireland, [2]School of Cosmic Physics, Dublin Institute for Advanced Studies, Dublin, Ireland, [3]Now at Department of Physics, Catholic University of America, Washington, DC, USA, [4]Now at NASA Goddard Space Flight Center, Space Weather Laboratory, Greenbelt, MD, USA, [5]Met Office, Exeter, UK, [6]British Geological Survey, Edinburgh, UK

Key Points:
- A new method for estimating geoelectric fields based on geomagnetic field time series and electromagnetic geophysical parameters is reported
- The method successfully reproduces electric and magnetic fields measured during both quiet and active time intervals in Ireland and the UK
- Modeled geoelectric fields accuracy depends on the distance to the closest magnetic observatory, and on the influence of local storms

Correspondence to:
J. Campanyà,
joan.campanya@tcd.ie

Citation:
Campanyà, J., Gallagher, P. T., Blake, S. P., Gibbs, M., Jackson, D., Beggan, C. D. et al. (2019). Modeling geoelectric fields in Ireland and the UK for space weather applications. *Space Weather*, *17*, 216–237. https://doi.org/10.1029/2018SW001999

Received 2 JUL 2018
Accepted 4 DEC 2018
Accepted article online 6 DEC 2018
Published online 5 FEB 2019

Abstract Geoelectric fields at the Earth's surface caused by geomagnetic storms have the potential to disrupt and damage ground-based infrastructure such as electrical power distribution networks, pipelines, and railways. Here we model geoelectric fields in Ireland and the UK during both quiet and active time intervals of geomagnetic conditions using measurements from magnetic observatories and electromagnetic tensor relationships. The analysis focused on (1) defining periods of the magnetic field variations that are largely affected by the geomagnetic storms, between 30 and 30,000 s; (2) constraining the electromagnetic tensor relationships that defines the Earth's response to magnetic field variations; (3) implementing and validating two approaches for modeling geoelectric fields based on measurements from magnetic observatories and local and interstation electromagnetic transfer functions; and (4) estimating uncertainties when modeling geoelectric fields. The use of interstation tensor relationships allowed us to differentiate between regional and local geomagnetic sources. We found coherence values of 0.5–0.95, signal-to-noise ratio of 1–15 dB, normalized root-mean-square values of 0.8–3.4, and root-mean-square values of 0.7–84 mV/km. Within these ranges of values, sites in close proximity (<100 km) to a magnetic observatory and not affected by local storms will provide the most accurate results, while sites located at further distances and affected by spatially localized features of the storm will be less accurate. These methods enable us to more accurately model geomagnetically induced currents, and their associated uncertainties, in the British and Irish power networks.

1. Introduction

The development of modern technologies and the adoption of renewable forms of energy and transportation is increasing the already high dependence of modern society both on electric power and on the robustness of our electrical infrastructure. One of the challenges to electrical infrastructure are geomagnetic storms, which can cause large variations in the Earth's magnetic fields and produce geoelectric fields at the Earth's surface. Geoelectric fields can interact with ground-based infrastructure generating induced electric currents, known as geomagnetically induced currents (GICs; Albertson & Thorson, 1974; Boteler & Pirjola, 2017; Pirjola, 2000; Pulkkinen et al., 2017).

Several studies highlight the potential risk of GICs damaging transformers and disrupting the power network, including the events in March 1989 in Canada (Allen et al., 1989; Béland & Small, 2004; Bolduc, 2002), in November 2001 in New Zealand (Marshall et al., 2012), and in October–November 2003 in South Africa (Gaunt & Coetzee, 2007; Koen & Gaunt, 2003). Larger geomagnetic storms than the events in 1989, 2001, and 2003 were observed at the beginning of the twentieth century and earlier (e.g., Cliver & Dietrich, 2013; Kappenman, 2005; Kataoka & Iwahashi, 2017), but the effects were less dramatic as society was not as dependent on electricity. The possibility of large economic losses for modern society associated with a large geomagnetic storm (e.g., Eastwood et al., 2017; Oughton et al., 2017) has increased the need for better understanding and characterization of the effects of geomagnetic storms on ground based infrastructures at low, middle, and high latitudes (Bailey et al., 2017; Barbosa et al., 2015; Ngwira et al., 2011; Torta et al., 2014; Torta et al., 2017; Zhang et al., 2015), and in particular in Ireland (Blake et al., 2016; Blake et al., 2018) and in the UK (Beggan et al., 2013; Kelly et al., 2017), which are the areas of interest for this study (Figure 1).

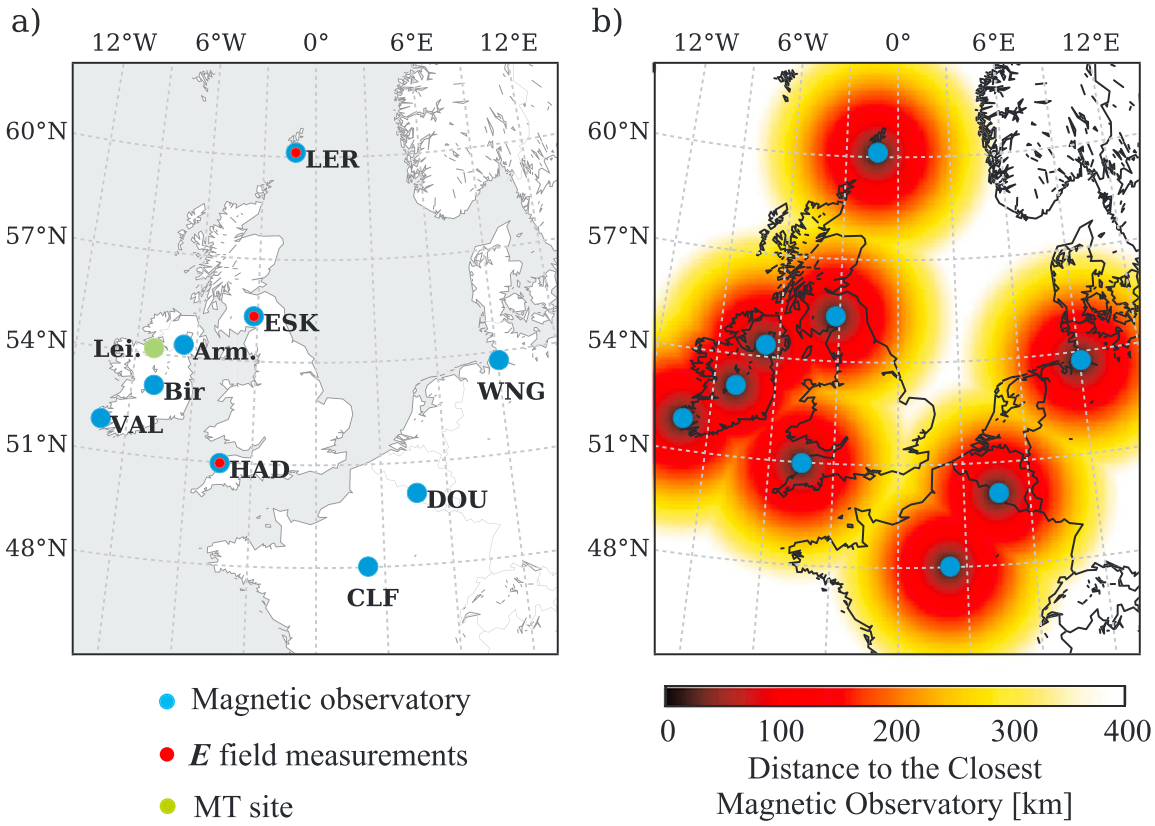

Figure 1. (a) Magnetic (blue circle) and electric (red circle) observatories used in this study. VAL, HAD, ESK, LER, CLF, DOU, and WNG are part of INTERMAGNET network. Bir and Arm are part of the MagIE Irish network. The green circle is a temporary magnetotelluric (MT) site that recorded electric and magnetic field variations during the first half of 2015. (b) Map showing the distance of any location in Ireland and the UK to the closest magnetic observatory.

A critical parameter for the study of GICs is the geoelectric fields at the Earth's surface caused by geomagnetic storms. The modeling of geoelectric fields, as a result of Earth's response to magnetic field variations, was performed in several studies assuming a homogeneous or a 1-D Earth for simplification. However, the complexity of the subsurface geology has motivated recent works to consider a more realistic 3-D Earth when estimating the geoelectric fields (Bonner & Schultz, 2017; Ivannikova et al., 2018; Kelbert et al., 2017; Weigel, 2017), which provides more accurate results when modeling the GICs (Torta et al., 2017).

The aim of this study is to evaluate the present possibilities for modeling the geoelectric fields in Ireland and the UK for space weather applications with two major objectives: (1) modeling the geoelectric fields during geomagnetic storms, including at sites where no measurements were made during the storm and (2) providing an error estimation for the modeled geoelectric time series with the aim of facilitating the estimation of error in the computed GICs. Two approaches, SECS-MT and SECS-ITF, based on state-of-the art geophysical methodologies were implemented and evaluated. In both approaches, the magnetic field variations were constrained using magnetic data from permanent magnetic observatories, and the response of the Earth to magnetic field variations was defined by electromagnetic tensor relationships considering a realistic 3-D Earth. SECS-MT employs spherical elementary current systems (SECS; Amm & Viljanen, 1999) to extrapolate the magnetic field variation between geomagnetic observatories with the geoelectric field computed using the measured MT impedance tensor. SECS-ITF is based on local and interstation electromagnetic transfer functions (ITF), again using SECS to extrapolate magnetic field variations. The use of interstation transfer functions allows SECS-ITF to separate the geomagnetic storms into two magnetic sources that we name *regional* and *local* geomagnetic signals, affecting either all of the sites in the area of study or only some of the sites, respectively.

Table 1a
Kp and Daily Ap Indices (www.swpc.noaa.gov) for Several Time Series During storm (S) Time

Storm days (*S*)	Maximum Kp/Ap	Quiet days (*Q*)	Maximum Kp/Ap
16/03/2013–18/03/2013	6/46	13/03/2013–15/03/2013	3/6
24/05/2013–26/05/2013	5/32	21/05/2013–23/05/2013	4/12
02/10/2013–04/10/2013	6/39	29/09/2013–01/10/2013	2/5
11/09/2014–13/09/2014	7/44	08/09/2014–10/09/2014	3/9
17/03/2015–19/03/2015	8/117	14/03/2015–16/03/2015	3/11
22/06/2015–24/06/2015	8/75	19/06/2015–21/06/2015	4/ 8

Note. Dates are formatted as dd-mm-yyyy.

2. Ireland and the UK Study Cases

2.1. Magnetic and Electric Field Measurements

Magnetic field variations in Ireland and the UK were recorded by the relatively high density network of magnetic observatories in Ireland (Valentia [VAL], Birr [Bir], and Armagh [Arm]), and in the UK (Hartland [HAD], Eskdalemuir [ESK], and Lerwick [LER]) and by the magnetic time series from Chambon la Foret (CLF), Dourbes (DOU), and Wingst (WNG) magnetic observatories in France, Belgium, and Germany, respectively (Figure 1). VAL, HAD, ESK, LER, CLF, DOU, and WNG are part of the INTERMAGNET network (www.intermagnet.org), and Birr and Armagh are part of the MagIE Irish network (www.rosseobservatory.ie). Electric field variations were recorded by the British Geological Survey (www.geomag.bgs.ac.uk) at the magnetic observatories in HAD, ESK, and LER between 2013 to present day using LEMI-701 systems designed by the Lviv Center of the Institute of Space Research (www.isr.lviv.ua) and Cu-$CuSO_4$ nonpolarizing electrodes. In addition, electric and magnetic time series from a temporary magnetotelluric (MT) station in Ireland (Leitrim, Lei) were also recorded during the first half of 2015 using LEMI-417 systems with $PbCl_2$ nonpolarizing electrodes.

2.2. Periods of Interest

The periods of the magnetic field variations that are largely affected by geomagnetic storms were constrained using magnetic time series from HAD, ESK and LER, each of which have a 1-s sampling rate and are distributed at different latitudes within the area of study (Figure 1). Magnetic field time series that are affected by geomagnetic storms were selected based on the planetary K index (Kp) and the Ap index. Kp is used to communicate the disturbance of the horizontal component of the magnetic field on a global scale. It is provided at 3-hr interval, calculated using 13 geomagnetic stations at latitudes between 44° and 60°, and the values range from 0 (low activity) to 9 (strong activity) in a quasi-logarithmic scale. The Ap index is based on Kp values but uses a linear scale instead of a quasi-logarithmic scale, ranges between 0 (low activity) and 400 (strong activity), and is an average of daily activity. For more detail about geomagnetic indices see Rostoker (1972). As the Kp and Ap indices are based on midlatitude observations, they are adequate parameters for selecting storm times in Ireland and the UK. In total, six geomagnetic storms between 2013 and 2016 with Kp index equal to or larger than 5 and daily Ap index greater than 30 were selected (Table 1a).

The impact of the geomagnetic storms on the Earth's surface magnetic fields was constrained by comparing, in the frequency domain, the 3 days of data affected by a geomagnetic storm with the 3 days of data prior to the geomagnetic storm following equation (1).

$$\mathrm{var}(T) = \frac{\sum_{i=1}^{m} |\boldsymbol{S}_i(T)| - \sum_{i=1}^{m} |\boldsymbol{Q}_i(T)|}{\sum_{i=1}^{m} |\boldsymbol{Q}_i(T)|} \quad (1)$$

where var represents the variations in the frequency domain, $\boldsymbol{S}$ is the spectra of the time series affected by geomagnetic storm, $\boldsymbol{Q}$ is the spectra of the time series previous to the geomagnetic storm, m is the number of analyzed storms, which is equal to 6 in this study, and T shows the period dependence of var, $\boldsymbol{S}$, and $\boldsymbol{Q}$.

Figure 2a shows the periods that are most affected by geomagnetic storms for the north-south component of the magnetic field, $\widetilde{\boldsymbol{B}}_x$, the east-west component of the magnetic field, $\widetilde{\boldsymbol{B}}_y$, and the total magnetic field, $\widetilde{\boldsymbol{B}}_T$. The x and y subscripts refer to orientation in geographic coordinates, following INTERMAGNET standards. The

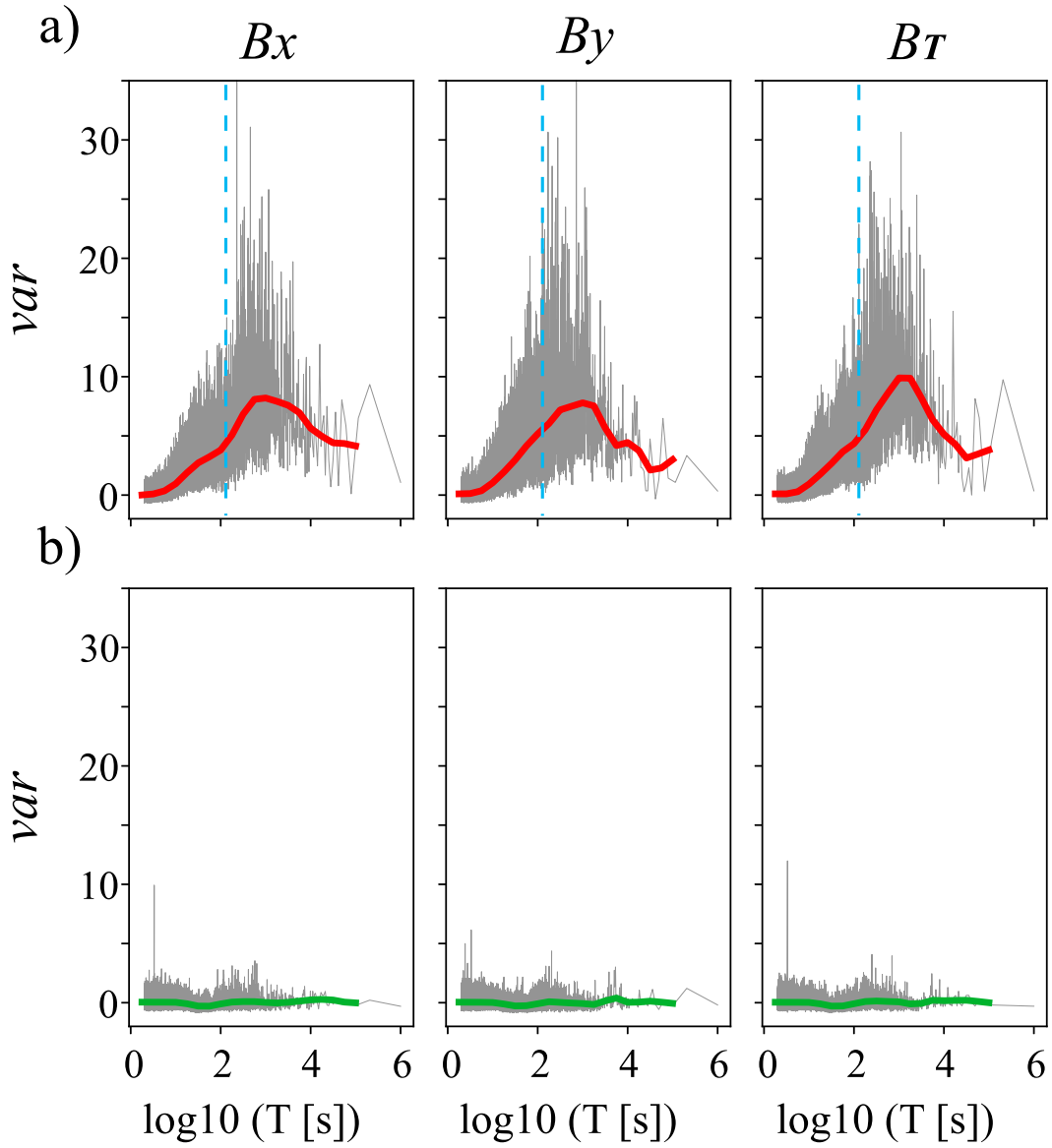

Figure 2. Analysis of the periods that are largely affected by geomagnetic storms. (a) Differences computed following (equation (1)) between horizontal magnetic time series affected by geomagnetic storm and horizontal magnetic time series prior to the geomagnetic storm. B_x is north-south component of the magnetic field, B_y is the east-west component of the magnetic field, and B_T represent the total horizontal magnetic field. Red line is a smooth version of the computed var. (b) Equivalent analysis comparing time series not affected by geomagnetic storms. Green line is a smooth version of the computed var. Vertical blue dashed line indicated the Nyquist limit when using 60-s sampling rate.

gray line represents the variations computed following equation (1), and the red line is a smooth version of the computed variations. The smooth line was constrained by selecting four periods per decade, equally spaced at $\log_{10}$ scale, and associating with each period of the smoothing curve the average value of all the periods between the previous and following periods of the smooth curve. If we integrate along the periods, using the red smooth curve, ~ 90% of the var signal can be explained by periods between 30 and 30,000 s, which are associated with var values larger than 2.

The reliability of the described approach was evaluated by computing the variations between quiet days (Table 1b). The results are shown in Figure 2b, in which the green line represent the smooth curve. Note that the green curves have var values smaller than 0.5.

In this study we focused on periods between 120 and 20,000 s, the shortest period being defined by the Nyquist limit for 60-s sampling rate, which is a common sampling rate for all of the sites used in this study,

Table 1b
Kp and Daily Ap Indices (www.swpc.noaa.gov) for Several Time Series During Quiet (Q) Time

Quiet days (Q_1)	Maximum Kp/Ap	Quiet days (Q_2)	Maximum Kp/Ap
04/01/2013–06/01/2013	2/3	01/01/2013–03/01/2013	1/3
19/04/2013–21/04/2013	2/4	16/04/2013–18/04/2013	2/3
18/01/2014–20/01/2014	1/3	15/01/2014–17/01/2014	2/9
24/11/2015–26/11/2015	1/3	21/11/2015–23/11/2015	3/4
03/12/2016–05/12/2016	2/4	30/11/2016–02/12/2016	2/4
15/12/2016–17/12/2016	3/6	12/12/2016–14/12/2016	3/6

Note. Dates are formatted as dd-mm-yyyy.

and the longest period being defined by the quality of the electromagnetic (EM) tensor relationships. Using this range of periods, ~78% of the var signal shown in Figure 2a can be explained. Measurements of the magnetic field variations using 1-s sampling rate, which is a current target for the INTERMAGNET standards, will allow us to model geoelectric fields for periods between 2 and 20,000 s, which captures ~93% of the var signal shown in Figure 2a. In order to extend the modeling of geoelectric fields to longer periods, the use of electrical resistivity models of the subsurface geology may help when the quality of the EM tensors relationships is not ideal. Torta et al. (2017) used 1-D MT modeling of each component of the impedance tensor, $\boldsymbol{Z}$, to extrapolate the impedance tensor to longer periods. The 1-D model was able to reproduce the measured component of the MT impedance tensor and, as the model propagates to infinite depth, allowed to extrapolate, as a first approach, the values of the MT impedance tensor at longer periods.

Although the selected periods are representative for the magnetic field variations, the primary source in this study, the periods of the geoelectric fields that are most affected by geomagnetic storm may vary significantly depending on the geoelectrical structures beneath the sites of interest. For example, Kelbert et al. (2017), working with geoelectric and geomagnetic data acquired in Japan, showed large peaks observed in the geoelectric fields associated with short periods (~10 s), which were not as obvious in the magnetic field time series.

2.3. Influence of the Electrical Properties of the Subsurface Geology

The subsurface geology and the coastal effects are known to have a key role when modeling geoelectric fields, and sharp changes have been observed at distances smaller than 70 km (e.g., Bedrosian & Love, 2015). In Ireland and the UK, the influence of the sea and the observed contrast in the geology at crustal and lithospheric scale (e.g., Jones & Hutton, 1979; Rao et al., 2007; Sule et al., 1993) suggest that large differences are to be expected between nearby sites.

EM transfer functions were used to model the response of the subsurface geology to magnetic field variations for the sites presented in Figure 1 including (1) the MT impedance tensor $\boldsymbol{Z}$, which describes the linear relationship between the horizontal components of the electric (E_x , E_y) and magnetic (B_x , B_y) fields measured at the same location; (2) the quasi-MT impedance tensor $\boldsymbol{Z'}$, which describes the linear relationship between the horizontal components of the electric fields measured at one site $\left(E_x^A, E_y^A\right)$ with the horizontal components of the magnetic field measured at a different site $\left(B_x^B, B_y^B\right)$, and (3) the horizontal magnetic transfer function $\boldsymbol{H}$, which describes the linear relationship between the horizontal components of the magnetic field measured at one site $\left(B_x^A, B_y^A\right)$ with the horizontal components of the magnetic field measured at a different site $(B_x^B, B_y^B$;Berdichevskiĭ & Dmitriev, 2008; Chave & Jones, 2012). For clarity, $\boldsymbol{Z}$ and $\boldsymbol{Z'}$ are described by equation (2), in which the superscript on top of the tensor identifies the location of the electric and magnetic fields, respectively. The MT impedance tensor is the particular case in which $A = B$. Note that this equation is equivalent to Faraday's law in the frequency domain, discarding the displacement current term as being negligible for the Earth conductivities and frequency ranges associated with GICs. The $\boldsymbol{H}$ tensor is described by equation (3), in which the superscript on top of the tensor identify the location of the magnetic fields measured at one site and the magnetic fields measured at a different site. If $A = B$, the $\boldsymbol{H}$ tensor would be the identity matrix.

$$\widetilde{\boldsymbol{E}}^A = \boldsymbol{Z}^{AB}\widetilde{\boldsymbol{B}}^B \tag{2}$$

$$\widetilde{\boldsymbol{B}}^A = \boldsymbol{H}^{AB}\widetilde{\boldsymbol{B}}^B \tag{3}$$

$\widetilde{\boldsymbol{E}}$ is the electric field, $\boldsymbol{Z}$ the MT impedance tensor or the quasi-MT impedance tensor, $\widetilde{\boldsymbol{B}}$ the magnetic field, and $\boldsymbol{H}$ is the horizontal magnetic tensor. The tilde (~) on top of the electric and magnetic fields symbolizes that we are in the frequency domain. Frequency dependence is assumed for $\widetilde{\boldsymbol{E}}$, $\widetilde{\boldsymbol{B}}$, $\boldsymbol{Z}$, and $\boldsymbol{H}$.

The EM tensor relationships used in this study were calculated using the Bounded Influence, Remote Reference Processing (BIRRP) processing algorithm (Chave & Thomson, 2004), applying the remote reference (RR) method (Gamble et al., 1979a, 1979b) and the ELICIT method (Campanya et al., 2014; Estimation of Local transfer-funtIons by Combining Inter-station Transfer-functions, ELICIT) during the processing of the data. The RR method uses correlated time series acquired at a remote site from the area of study to reduce the influence of correlated and uncorrelated noise at the site of interest, having the capacity to reduce bias and source effects of correlated noise. Data from magnetic observatories located at more than 500 km from the sites of interest were considered for RR. One of the main issues associated with RR is that the performance decreases for longer periods as the number of samples reduces. The ELICIT method, based on interstation tensor relationships between electric and magnetic fields measured at different locations, was used to consider the good quality segments of the time series without the need of the electric and magnetic fields at the site of interest to be acquired simultaneously, thus increasing the number of samples when processing the data.

For processing the data, we selected 30 days of 1-s measurements acquired between 2013 and 2015 ensuring the presence of days with moderate geomagnetic activity. This was performed to derive a statistically meaningful set of signals for each of the periods of interest. As the tensor relationships are valid under the assumption of the plane wave approximation, days affected by large geomagnetic storms (Kp $>$ 4) were not considered as we wish to avoid local source effects related to strong ionospheric currents, in particular for the sites located further north. The time series for computing the tensor relationships were not later used to evaluate the presented approaches for modeling geoelectric fields.

As an illustration, Figure 3a shows the impedance tensors relating the electric field variations from ESK and Lei to the magnetic field variations from several magnetic observatories. As Lei is a nonpermanent site, magnetic time series from Lei were only used to calculate its local MT impedance tensor. The plots in Figure 3a highlight the significant differences depending on the magnetic field data used to constrain the tensor relationship, suggesting that the electrical properties beneath different sites varies significantly. Figure 3b shows the $\boldsymbol{H}$ tensor relationships relating the magnetic field variations at several magnetic observatories to the magnetic field variations from CLF. The CLF site was selected as the reference as is the least likely to be affected by local geomagnetic storms, which will be relevant for SECS-ITF approach. Deviations away from the identity matrix are related to the different geoelectric structures beneath the magnetic observatories.

In general, larger differences are observed for shorter periods, which are associated with shallower structures, while for longer periods, associated with deeper structures, differences are reduced suggesting a similar geoelectric environment. Although modeling will be required to accurately estimate the depth of penetration for different periods the concept of skin depth, equation (4) can be considered as a first approximation. The skin depth describes the depth at which an electromagnetic wave with angular period, T, will penetrate into a medium with a homogeneous electrical resistivity, ρ, before its amplitude is attenuated by a factor of 1/e (i.e., Chave & Jones, 2012).

$$\delta \approx 500\sqrt{\rho T} \tag{4}$$

From the skin depth it can be seen that shorter periods attenuate at shallower depths than longer periods, and that the waves will also attenuate quicker when propagating though materials with low electrical resistivity values.

For all of the computed EM tensor relationships the quality of the data was reasonable for periods between 120 and 20,000 s, including the main periods of interest for the analysis of geomagnetic storms presented in Figure 2. Note that VAL, DOU, and WNG magnetic observatories provided 60-s sampling rate, which means that because of the Nyquist limit no results are available for periods shorter than 120 s. Poor quality or missing points in the electromagnetic tensor relationships associated with periods between 120 and 20,000 s were replaced by interpolated values using nearby periods with good quality data. The interpolated values were less than 2% of the total analyzed data.

3. Theory

Modeling geoelectric fields at the Earth's surface requires an accurate knowledge of the magnetic field variations, and of the Earth's response to these variations. The magnetic field variations were measured at the

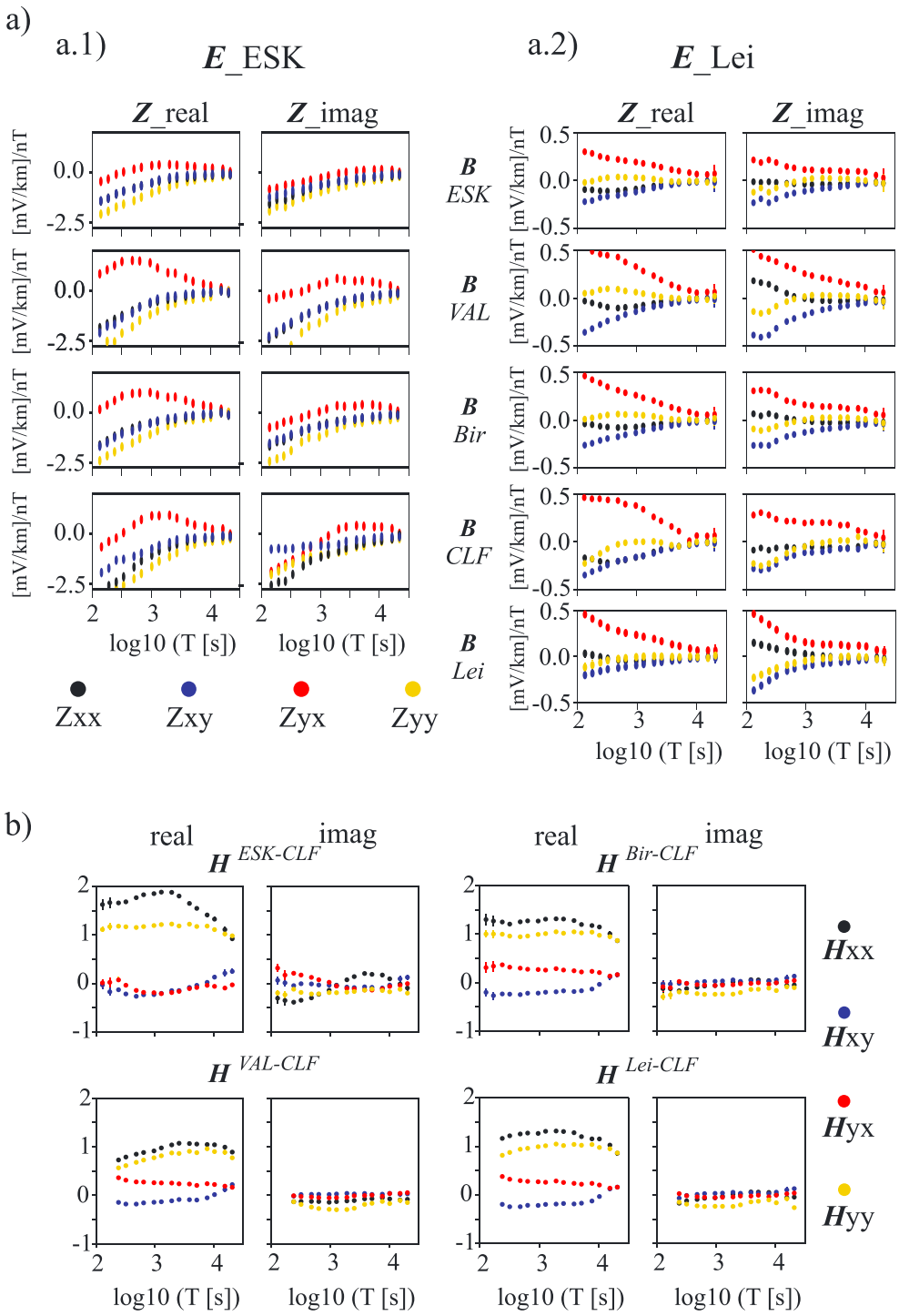

Figure 3. (a1 and a2) Electromagnetic tensor relationships, for periods between 100 and 20,000 s, relating the electric fields, ***E***, measured at (a1) ESK and at (a2) Lei to the magnetic fields, ***B***, measured at several sites (HAD, ESK, LER, VAL, CLF, Bir, Arm, and Lei). (b) Horizontal magnetic tensor relationship, ***H***, for periods between 100 and 20,000 s relating the magnetic fields, ***B***, at the magnetic observatories shown in Figure 1, to the magnetic fields at CLF. Black, blue, red, and yellow circles represent the components of the tensor relationship. HAD = Hartland; VAL = Valentia; ESK = Eskdalemuir; LER = Lerwick; VAL = Valentia; CLF = Chambon la Foret; Bir = Birr; Arm = Armagh; Lei = Leitrim.

magnetic observatories (Figure 1), and interpolated to nearby locations using the spherical elementary current system (Amm & Viljanen, 1999). SECS assumes that the varying component of the magnetic field on the ground can be represented by a system of divergence-free equivalent currents in the ionosphere. These equivalent currents are solved for true input magnetic data at the Earth surface, that is, at the magnetic observatories. The magnetic field at any point on the ground, within the region defined by the magnetic observatories, can then be calculated as the sum of magnetic effects from these constructed currents. Recent studies in Ireland and in the UK already used SECS as a reasonable approach for interpolating magnetic field variations between magnetic observatories (e.g., Blake et al., 2016; Kelly et al., 2017). The Earth's response to the magnetic field variations, the geoelectric fields, was constrained using EM tensor relationships considering a realistic 3-D Earth.

We first describe the modeling of geoelectric fields when the magnetic field variations at the site of interest are measured. Then, we present two approaches for modeling geoelectric fields at sites between magnetic observatories, when interpolation of the magnetic field variations is required.

3.1. Known Magnetic Field Variations at the Site of Interest

In the hypothetical case that the magnetic data were recorded at the site of interest, *A*, the geoelectric fields can be constrained, in the frequency domain, following equation (5):

$$\widetilde{\boldsymbol{E}}^{A} = \boldsymbol{Z}^{AA}\widetilde{\boldsymbol{B}}^{A} \tag{5}$$

The superscript indicates the site in which the fields were recorded, in this example site *A*. Note that this is equivalent to equation (2) with $A = B$.

3.2. Unknown Magnetic Field Variations at the Site of Interest

Two approaches, SECS-MT and SECS-ITF, were tested for modeling geoelectric fields at a site where no direct measurements of the magnetic field variations were performed during the geomagnetic storm. Figure 4 shows a diagram with the main steps followed by the two approaches.

3.2.1. SECS-MT: Based on SECS and on the MT Impedance Tensor (Z)

Following this approach the magnetic field variations at the site of interest, *A*, were calculated by interpolating the magnetic field variations measured at the magnetic observatories using SECS (equation (6)).

$$\dot{\boldsymbol{B}}^{A} = \mathrm{SECS}\left[\boldsymbol{B}^{1}, \boldsymbol{B}^{2}, \ldots, \boldsymbol{B}^{s}\right] \tag{6}$$

where $\boldsymbol{B}$ is the magnetic field variations in the time domain and the superscript from 1 to *s* represent the nearby stations were the magnetic field variations were recorded, for example, in the permanent magnetic observatories. The accent (dot) symbolizes that the magnetic field was computed as a result of the SECS interpolation process.

We take the fast Fourier transform (FFT) of the time series and use the spectra of the resulting magnetic field variations (from equation (6)) multiplied by the MT impedance tensor in the frequency domain to compute the spectra of the geoelectric fields (equation (7)).

$$\boldsymbol{E}^{A} \approx \mathrm{FFT}^{-1}\left[\boldsymbol{Z}^{\boldsymbol{AA}} \cdot \mathrm{FFT}\left[\dot{\boldsymbol{B}}^{A}\right]\right] \tag{7}$$

where $\boldsymbol{E}$ is the electric field variations at site *A* in the time domain, FFT is the fast Fourier transform, and FFT^{-1} the inverse of the fast Fourier transform. Note that the length of the FFT was matched to the frequency bandwidth of the tensor relationship, between 120 and 20,000 s, including the periods of interest.

3.2.2. SECS-ITF: Based on the SECS and on Local and ITF

This approach assumes that the geomagnetic storms can be separated into two magnetic sources that we name the *regional* and *local* geomagnetic signals. The *regional* signal represents a magnetic source that is the same for the whole area of study, in our case the region shown in Figure 1. The *local* signal is the part of the geomagnetic storm that is not represented by the *regional* signal, and it is related to geomagnetic sources that only affect some of the magnetic observatories. *Regional* signals can be related to sudden impulses, magnetospheric (ring currents), and homogeneous ionospheric currents above the area of study. An example of *local* signal would be the ionospheric currents associated with the electrojet, which will

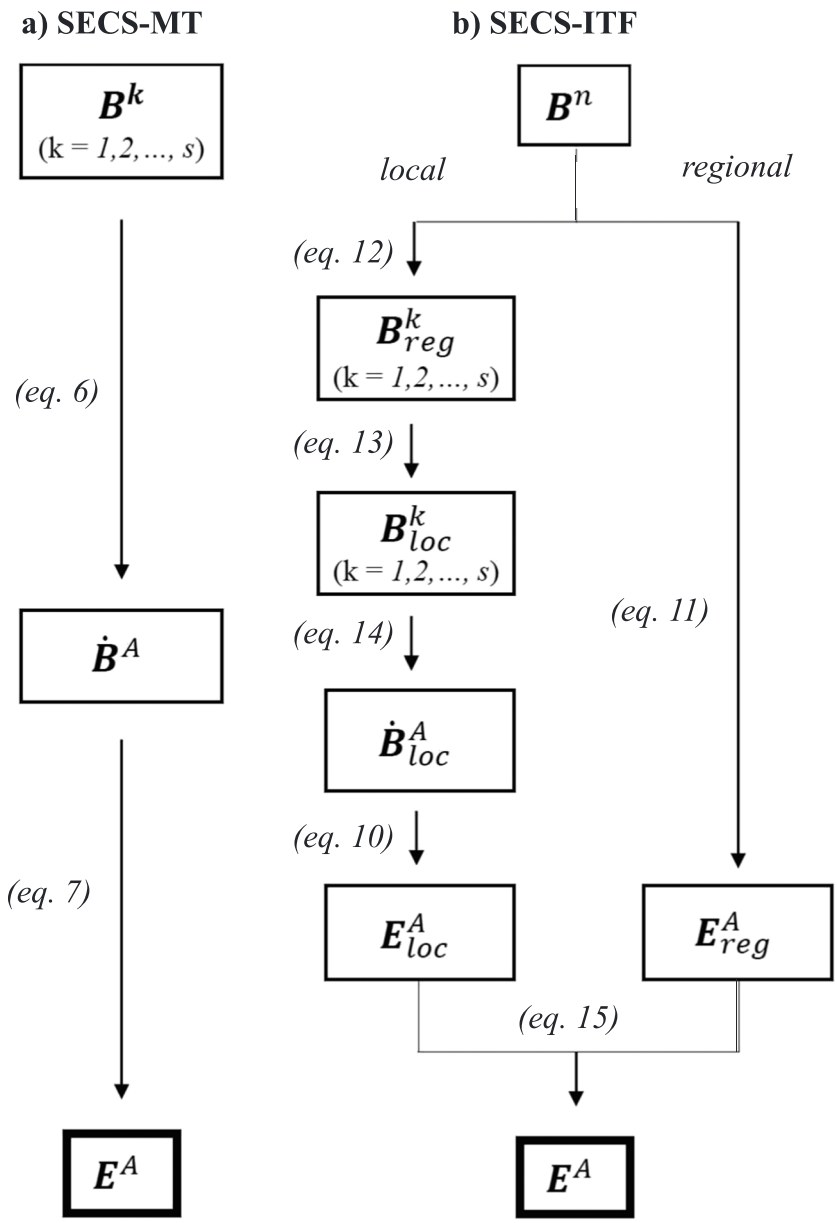

Figure 4. Diagram showing the main steps followed by (a) SECS-MT and (b) SECS-ITF to compute geoelectric fields. Equations of each step makes reference to the equations described in the text.

more strongly affect sites that are closer to the electrojet than the sites located further away. Under this assumption, equation (5) can be expressed as equation (8)

$$\tilde{\boldsymbol{E}}^{\boldsymbol{A}} = \tilde{\boldsymbol{E}}^{A}_{\mathrm{reg}} + \tilde{\boldsymbol{E}}^{A}_{\mathrm{loc}} = \boldsymbol{Z}^{AA}\left(\tilde{\boldsymbol{B}}^{A}_{\mathrm{reg}} + \tilde{\boldsymbol{B}}^{A}_{\mathrm{loc}}\right) = \boldsymbol{Z}^{AA}\tilde{\boldsymbol{B}}^{A} \tag{8}$$

where the subindex reg and loc refers to the regional and local signals, respectively. Following this approach equation (8) can be separated into equations (9) and (10).

$$\boldsymbol{E}^{A}_{\mathrm{reg}} = \mathrm{FFT}^{-1}\left[\boldsymbol{Z}^{AA}\cdot\mathrm{FFT}\left[\boldsymbol{B}^{A}_{\mathrm{reg}}\right]\right] \tag{9}$$

$$\boldsymbol{E}^{A}_{\mathrm{loc}} = \mathrm{FFT}^{-1}\left[\boldsymbol{Z}^{AA}\cdot\mathrm{FFT}\left[\boldsymbol{B}^{A}_{\mathrm{loc}}\right]\right] \tag{10}$$

Regional signal (equation (9)) works under the assumption of the plane wave approximation. This means that the regional electric and magnetic field at the site of interest ($\boldsymbol{E}^{A}_{\mathrm{reg}}, \boldsymbol{B}^{A}_{\mathrm{reg}}$) can be constrained by the magnetic

fields at a nearby station using the interstation transfer functions. If we assume that there is a neighboring site, n, not affected by local storms, $\boldsymbol{E}^A_{\text{reg}}$ and $\boldsymbol{B}^A_{\text{reg}}$ can be modeled using the magnetic field data measured at site n, $\boldsymbol{B}^n$ (equations (11) and (12)).

$$\boldsymbol{E}^A_{\text{reg}} = \text{FFT}^{-1}\left[\boldsymbol{Z}^{An}\cdot\text{FFT}[\boldsymbol{B}^n]\right] \tag{11}$$

$$\boldsymbol{B}^A_{\text{reg}} = \text{FFT}^{-1}\left[\boldsymbol{H}^{An}\cdot\text{FFT}[\boldsymbol{B}^n]\right] \tag{12}$$

Recent results from Wang et al. (2017) already demonstrate the accuracy of equations (11) and (12) at modeling the natural electric and magnetic fields when the plane wave approximation is valid, showing coherence values above 0.96, and signal-to-noise ratio (SNR) values larger than 10 dB. This means that following equations (11) and (12), we can directly calculate $\boldsymbol{E}^A_{\text{reg}}$ and $\boldsymbol{B}^A_{\text{reg}}$ from $\boldsymbol{B}^n$, modeling the contribution of the regional signal at site A.

The local signal at the magnetic observatories, $\boldsymbol{B}^k_{\text{loc}}$ (for $k = 1, \ldots, s$) can be calculated by removing the contribution of the regional magnetic signal (equation (12)) from the measured magnetic field at the magnetic observatories following (equation (13)).

$$\boldsymbol{B}^k_{\text{loc}} = \boldsymbol{B}^k - \boldsymbol{B}^k_{\text{reg}} = \boldsymbol{B}^k - \text{FFT}^{-1}\left[\boldsymbol{H}^{kn}\widetilde{\boldsymbol{B}}^n\right] \qquad \text{for } k = 1, \ldots, s \tag{13}$$

where s is the number of magnetic observatories in the area of study and n is a magnetic observatory not affected by local storms. Once the local signal at each magnetic observatory is calculated, SECS can be applied to interpolate the contribution of the local signal at site A (equation (14)).

$$\dot{\boldsymbol{B}}^A_{\text{loc}} = \text{SECS}\left[\boldsymbol{B}^1_{\text{loc}}, \boldsymbol{B}^2_{\text{loc}}, \ldots, \boldsymbol{B}^s_{\text{loc}}\right] \approx \boldsymbol{B}^A_{\text{loc}} = \boldsymbol{B}^A - \text{FFT}^{-1}\left[\boldsymbol{H}^{An}\widetilde{\boldsymbol{B}}^n\right] \tag{14}$$

Combining equation (10) to equation (14) results in equation (15), which allows us to model the geoelectric fields at site A using magnetic data from neighboring stations.

$$\boldsymbol{E}^A = \boldsymbol{E}^A_{\text{reg}} + \boldsymbol{E}^A_{\text{loc}} = \text{FFT}^{-1}\left[\boldsymbol{Z}^{An}\cdot\text{FFT}(\boldsymbol{B}^n)\right] + \text{FFT}^{-1}\left[\boldsymbol{Z}^{AA}\cdot\text{FFT}(\dot{\boldsymbol{B}}^A_{\text{loc}})\right] \tag{15}$$

The presented approach (equation (15)) assumes that there is at least one magnetic observatory not affected by local storms, site n, but this may not always be the case and all stations may be affected by local effects at different levels. Below, we analyze the influence of having a local signal at site n when applying equation (15). In this case equation (14) will be written as equation (16), and equation (15) would become equation (17).

$$\dot{\boldsymbol{B}}^A_{\text{loc}} \approx \boldsymbol{B}^A - \text{FFT}^{-1}\left[\boldsymbol{H}^{An}\widetilde{\boldsymbol{B}}^n\right] = \boldsymbol{B}^A - \text{FFT}^{-1}\left[\boldsymbol{H}^{An}\left(\widetilde{\boldsymbol{B}}^n_{\text{reg}} + \widetilde{\boldsymbol{B}}^n_{\text{loc}}\right)\right] \tag{16}$$

$$\widetilde{\boldsymbol{E}}^A = \boldsymbol{Z}^{An}\left(\widetilde{\boldsymbol{B}}^n_{\text{reg}} + \widetilde{\boldsymbol{B}}^n_{\text{loc}}\right) + \boldsymbol{Z}^{AA}\left(\widetilde{\boldsymbol{B}}^A - \left(\boldsymbol{H}^{An}\left(\widetilde{\boldsymbol{B}}^n_{\text{reg}} + \widetilde{\boldsymbol{B}}^n_{\text{loc}}\right)\right)\right) \tag{17}$$

Equation (17) can be simplified by combining the tensor relationships that are multiplying between them, such as shown in equation (18) (see García & Jones, 2005; Campanya et al., 2014, for more detail on combining EM tensor relationships).

$$\boldsymbol{Z}^{An} = \boldsymbol{Z}^{AA}\boldsymbol{H}^{An} \tag{18}$$

Simplification of equation (17) shows that it is equivalent to equation (8), the only difference being the accuracy of constraining $\boldsymbol{B}^A_{\text{loc}}$ through the SECS interpolation method.

This result demonstrates that the presence of local signal at site n may not be an issue when modeling the electric fields at site A. However, the accuracy of the approach is dependent on the accuracy of SECS at interpolating the local magnetic field variations when calculating $\boldsymbol{B}^A_{\text{loc}}$. Taking this limitation in consideration, choosing a reference site at lower latitudes, less affected by local signals, should facilitate the performance of this approach as no artificial geomagnetic sources will need to be created to compensate for local signals affecting the reference site but not the other sites, for example at lower latitudes.

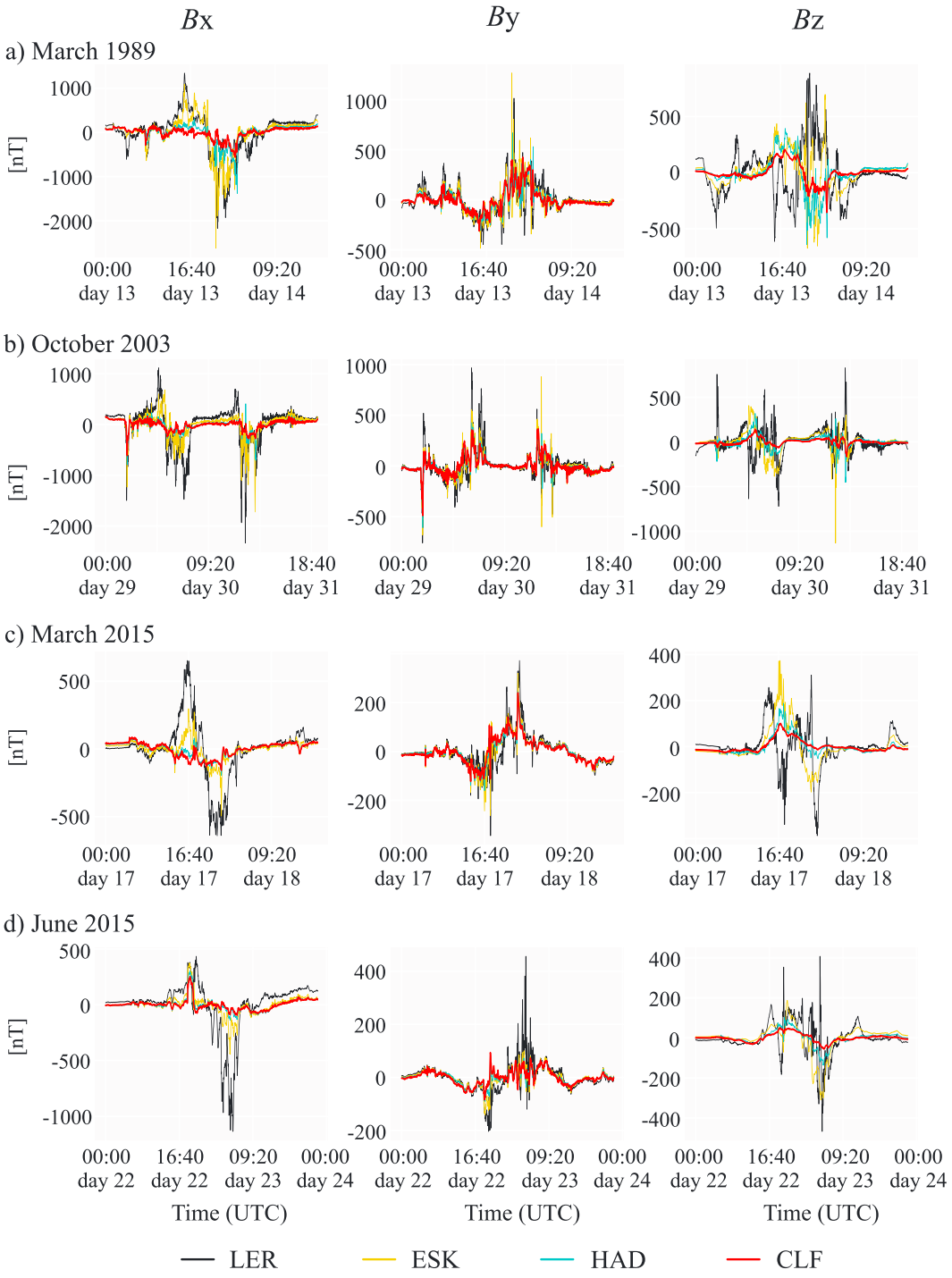

Figure 5. North-south, B_x, east-west, B_y, and vertical B_z, components of the magnetic fields measured at CLF (red), HAD (blue), ESK (yellow), and LER (black) during several large geomagnetic storms: (a) 13–14 of March 1989, (b) 29–31 of October 2003, (c) 17–18 of March 2015, and (d) 22–23 of June 2015. CLF = Chambon la Foret; HAD = Hartland; VAL = Valentia; ESK = Eskdalemuir; LER = Lerwick.

CLF magnetic observatory (Figure 1), the most southerly data set, was selected as a magnetic observatory assumed to be unaffected by local effects, site *n*, as it is expected to be less affected by the influence of the auroral electrojet, usually the major source of local effects. Figure 5 shows the magnetic fields variations at LER, ESK, HAD, and CLF for four large geomagnetic storms, including the 1989 storm. Looking at the

horizontal components, B_x and B_y, x for north-south and y for east-west directions, CLF had the smallest variations. Sites located at higher latitudes were affected by additional signals and larger variations were observed. If we focus on the vertical component of the magnetic field variations, B_z, if there is no presence of local signals, the variations of B_z are associated with induced magnetic fields caused by the subsurface geology, which are usually relatively small in comparison with the magnetic source. However, under the influence of local geomagnetic sources, large vertical magnetic field variations can be observed, in particular at the edge of the main ionospheric currents (Boteler & Pirjola 1998; Johnsen, 2013). For the presented examples, CLF also shows the smallest variations for B_z during geomagnetic storms corroborating the idea that CLF is less affected by local geomagnetic sources than HAD, ESK, and LER magnetic observatories.

3.3. Parameters for Evaluating the Performance at Modeling Geoelectric Fields

Coherence (Coh, equation (19)), SNR (equation (20)), root-mean-square (RMS, equation (21)), and the normalized root-mean square (nRMS, equation (22)) were used to evaluate the accuracy when modeling geoelectric fields.

$$\mathrm{Coh} = \frac{\sum_{i=1}^{N}\left(\boldsymbol{E}_{\mathrm{data}\,i} - \overline{\boldsymbol{E}}_{\mathrm{data}}\right)\left(\boldsymbol{E}_{\mathrm{mod}\,i} - \overline{\boldsymbol{E}}_{\mathrm{mod}}\right)}{\sqrt{\sum_{i=1}^{N}\left(\boldsymbol{E}_{\mathrm{data}\,i} - \overline{\boldsymbol{E}}_{\mathrm{data}}\right)^2 \sum_{i=1}^{N}\left(\boldsymbol{E}_{\mathrm{mod}\,i} - \overline{\boldsymbol{E}}_{\mathrm{mod}}\right)^2}} \tag{19}$$

$$\mathrm{SNR} = 10\log_{10}\frac{\sum_{i=1}^{N}\boldsymbol{E}_{\mathrm{data}\,i}^{2}}{\sum_{i=1}^{N}\left(\boldsymbol{E}_{\mathrm{data}\,i} - \boldsymbol{E}_{\mathrm{mod}\,i}\right)^2} \quad (\mathrm{dB}) \tag{20}$$

$$\mathrm{RMS} = \sqrt{\frac{1}{N}\sum_{i=1}^{N}\left(\boldsymbol{E}_{\mathrm{mod}\,i} - \boldsymbol{E}_{\mathrm{data}\,i}\right)^2} \tag{21}$$

$$\mathrm{nRMS} = \frac{\sqrt{\frac{1}{N}\sum_{i=1}^{N}\left(\boldsymbol{E}_{\mathrm{mod}\,i} - \boldsymbol{E}_{\mathrm{data}\,i}\right)^2}}{\frac{1}{N}\sum_{i=1}^{N}\sigma_i} \tag{22}$$

where $\boldsymbol{E}_{\mathrm{data}}$ is the measured geoelectric fields and $\boldsymbol{E}_{\mathrm{mod}}$ the modeled geoelectric fields, $\overline{\boldsymbol{E}}_{\mathrm{data}}$ and $\overline{\boldsymbol{E}}_{\mathrm{mod}}$ represent the average values of the geoelectric fields, σ is the standard deviation of the modeled geoelectric fields and associated with the errors at modeling geoelectric fields, and N is the number of data points in the time series.

The Coh values, invariant in scale, were used to evaluate similarities between time series focusing on the variations but without taking into account the amplitude of the signal. Values close to one indicated that the two time series vary in a similar manner. The SNR between the measured and the residual time series was used to quantify the similarity between time series by taking into account the power of the signal. Positive SNR values indicate that the power of the signal is larger than the residuals, and SNR values larger than 10 indicate that the power of the signal is more than 10 times larger than the residuals. The RMS was used to quantify differences between measured and modeled time series, and the nRMS to quantify the differences between measured and modeled time series taking into account the estimated errors of the modeled geoelectric fields. A poor result from Coh, SNR, or RMS would indicate that the recovered time series were not accurate at defining the measured geoelectric fields. nRMS values significantly smaller or larger than unity would indicate that the estimated errors were not accurate.

4. Method Implementation and Validation

4.1. Method Implementation

The presented approaches for modeling geoelectric fields were implemented by defining the main errors to be considered when modeling geoelectric fields in Ireland and the UK and by modeling the geoelectric fields at Lei (a site relatively close to the closest magnetic observatory, ~100 km from Armagh) and at ESK (a site relatively far away from the closest magnetic observatory, ~250 km from Armagh) during the geomagnetic storm in 22–23 August 2015.

4.1.1. Error Estimation

Three types of errors were considered when modeling the electric and magnetic time series during geomagnetic storms related to (1) errors from the tensor relationships, (2) the assumption of the plane wave approximation, and (3) the accuracy of interpolating magnetic field variations using SECS. As the errors are based on data from the area of study (Figure 1), the presented values may not be adequate for other regions, in particular the errors associated with the accuracy at interpolating the magnetic field variations using SECS. Equivalent analysis should be performed in other regions when aiming to estimate the errors for the SECS-MT and SECS-ITF approaches.

4.1.1.1. Errors From the Tensor Relationships

The errors related to the tensor relationships were defined when processing the data to obtain $\boldsymbol{Z}$ and $\boldsymbol{H}$. In addition, to avoid the influence of small errors caused by poor statistics, an error floor, that is, minimum error for each component of the tensor relationships, was imposed. The error floor was defined by modeling the electric fields at ESK, HAD, LER, and Lei sites using time series not affected by large geomagnetic storms. In this study we selected the three days of data previous to the geomagnetic storms in 17–18 March 2015 and in 22–23 June 2015. The largest error floor that returned the smallest nRMS values above a value of 1, for all of the sites, was selected. Following this approach we imposed an error floor of 10% on the components of $\boldsymbol{Z}$, and 0.02 in absolute value on the components of $\boldsymbol{H}$. The nRMS values from modeling geoelectric fields, considering the errors from the tensor relationships and imposing the error floor, were between 1.0 and 3.2, while the RMS values ranged between 0.3 and 14.8 mV/km.

4.1.1.2. Errors Associated With the Assumption of the Plane Wave Approximation During Geomagnetic Storms

The MT impedance tensor, $\boldsymbol{Z}$, works under the assumption of plane wave approximation, which is not entirely valid during strong geomagnetic storms (e.g., Romano et al., 2014; Varentsov et al., 2003). This means that during geomagnetic storms $\boldsymbol{Z}$ may not reproduce the Earth's response to the magnetic field variations with the same accuracy as during quiet times. Note, however, that previous results have already shown reasonable accuracy values, 5% to 10% error, at modeling geoelectric time series during geomagnetic storms when the magnetic field variations at the site of interest are known (Kelbert et al., 2017).

The error associated with the assumption of the plane wave approximation was defined by modeling the electric fields at ESK, HAD, LER and Lei sites during the 17–18 March 2015 and the 22–23 June 2015 geomagnetic storms. The differences between modeled and measured electric fields were evaluated using SNR, as larger errors were observed for larger signals. The SNR between modeled and measured electric time series was computed for HAD, ESK, LER, and Lei sites using the magnetic time series measured at the site of interest, thus avoiding additional errors related with the interpolation methods. The average SNR values was around 10 dB.

Based on this analysis, an error was added in the spectra of the modeled geoelectric fields, considering a random normal deviation with sigma equal to 0.31 times the value of the spectra for each period, which is equivalent to a SNR of 10 dB. By considering this error, in combination with the errors from the tensor relationships, the nRMS at the four observatories for the two selected storms ranged between 0.9 and 3.4, while the RMS values ranged between 1.2 and 84 mV/km. Note that if only the errors from the tensor relationships were considered, ignoring the errors presented in this subsection, the nRMS values would had range between 2.1 and 7.5.

4.1.1.3. Errors From Interpolating Magnetic Field Variations Using SECS

A similar approach to that in the previous subsection, based on the SNR, was performed to define the errors related to the interpolation of the total, SECS-MT, and the local, SECS-ITF, magnetic field variations using SECS. The magnetic field variations at ESK, HAD, Lei, and Bir for the same two storms were computed following SECS interpolation method using several combinations of magnetic observatories including all the sites presented in Figure 1. When applying SECS for interpolating magnetic field variations, there should always be magnetic observatories surrounding the site of interest. Because of this limitation, data from LER magnetic observatory was not considered for this analysis as it is at the northernmost edge. Coh and SNR values from interpolating the total and local magnetic field variations in relation to the distance to the closest magnetic observatory are shown in Figure 6.

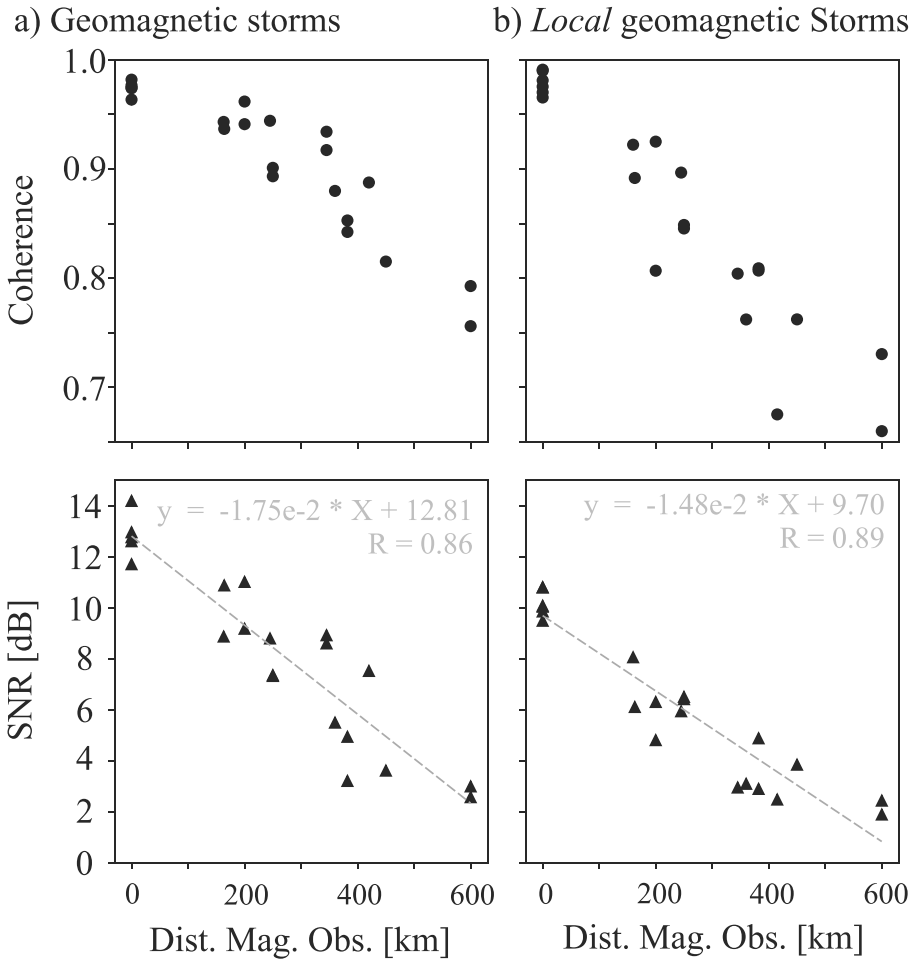

Figure 6. Error analysis, focusing on coherence and signal-to-noise ratio, from interpolating the magnetic field variations using the spherical elementary current system. The gray line is a linear fit of the signal-to-noise ratio (SNR) representing the decrease in resolution as the site is located far away from the closest magnetic observatory. (a) Error analysis at interpolating the total magnetic field variations. (b) Error analysis at interpolating the magnetic field variations of the local component of the geomagnetic storm.

Both Coh and SNR show a decrease in accuracy as the site of interest distances from the closest magnetic observatory. Focusing on the SNR values (Figure 6, lower panels), and for the range of distances evaluated in this study, a linear relationship between SNR and the distance to the closest observatory is suggested (gray lines). Based on this linear relationship, errors were added to the interpolated magnetic field variations resulted from SECS. Note that SNR use a logarithmic scale (dB), which means that the error increases exponentially with the distance. Based on the results from Figure 6, during large geomagnetic storms negative SNR values can be expected when the distance between the site of interest and the closest magnetic observatory is (1) more than 730 km when modeling the total magnetic field variations and (2) more than 650 km when modeling the magnetic field variations caused by local storms. Negative SNR values indicate that the errors are larger than the signal.

The nRMS values at interpolating the total and local magnetic field variations ranged between 1.3 and 3.7, while the RMS values ranged between 11.9 and 34.9 nT. This range of misfit values is in agreement with the misfit values observed by McLay and Beggan (2010) interpolating the magnetic field variations at ESK using SECS during the geomagnetic storm of 11 September of 2005.

4.1.2. Modeling Geoelectric Fields

The proposed methodologies, SECS-MT and SECS-ITF, were implemented by modeling the geoelectric fields at Lei and ESK during the 22–23 June 2015 geomagnetic storm considering the errors described above. The

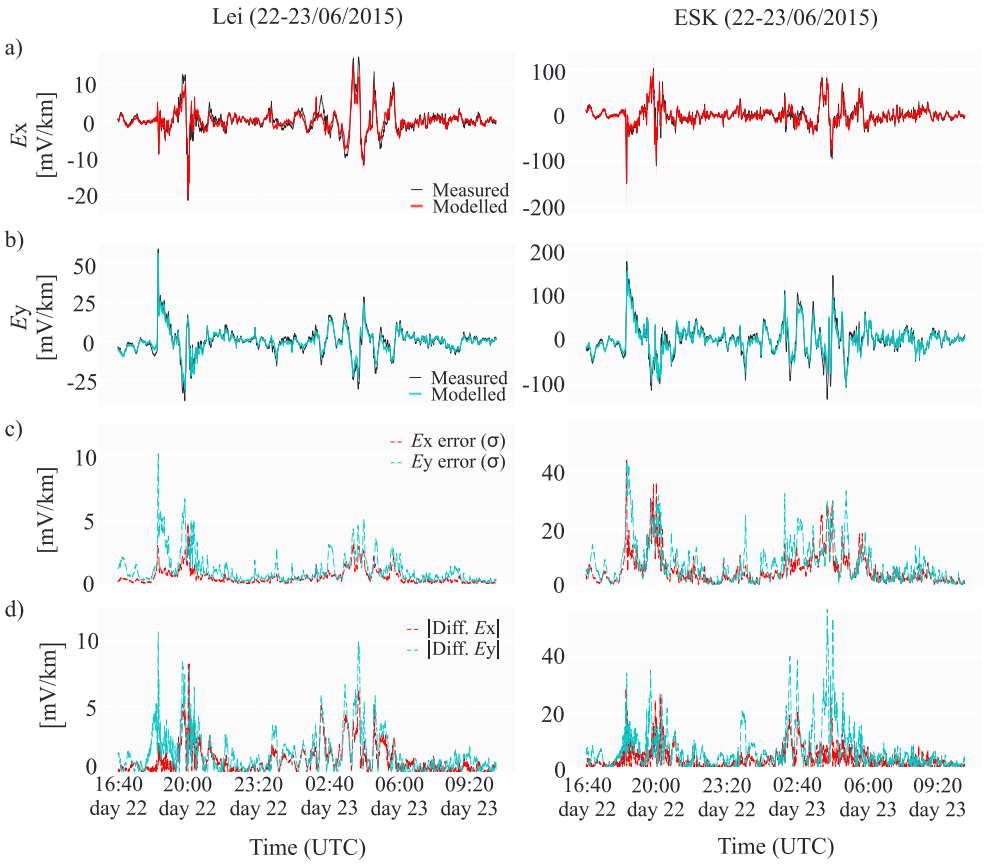

Figure 7. Modeled geoelectric fields at Lei and ESK during the geomagnetic storm in June 2015 under the assumption that the magnetic field variations at the sites of interest were known (equation (4)). (a) The *x* (north-south) component of the geoelectric fields. Black is measured geoelectric fields and red modeled geoelectric fields (b) *y* (east-west) component of the geoelectric fields. Black is measured geoelectric field and blue modeled geoelectric fields. (c) Estimated errors at computing geoelectric fields, red for *x* component and blue for *y* component. (d) Differences between modeled and measured geoelectric fields. Red for *x*-component and blue for *y* component. Lei = Leitrim; ESK = Eskdalemuir.

errors were propagated using 1,000 random samples normally distributed among the mean value with a standard deviation defined by the errors. The modeled geoelectric time series and the estimated errors were defined as the mean value and as the standard deviations of the calculated geoelectric time series, respectively.

The modeling of the geoelectric fields was first tested assuming that the magnetic field variations of the site of interest were known (Figure 7). Then, SECS-MT and SECS-ITF were considered assuming that there were no measurements at the site of interest during the geomagnetic storm (Figure 8). Figures 7 and 8 compares measured (black lines) and modeled (color lines) *x*, north-south, and *y*, east-west, components of the geoelectric field, and provides an estimate of the errors in the modeled geoelectric fields and of the differences between the modeled and measured geoelectric fields (color dashed lines). When the magnetic field variations were known (Figure 7) the fit of the data showed Coh values between 0.94 and 0.97, SNR values between 9 and 12 dB, RMS values between 1 and 10 mV/km, and nRMS values between 1.3 and 2.0, having similar results for ESK and Lei. When the magnetic field variations at the site of interest were not known and the geoelectric fields were modeled following SECS-MT or SECS-ITF (Figure 8) the fit of the data showed Coh values between 0.77 and 0.95, SNR values between 3.8 and 10.0, RMS values between 1 and 24 mV/km, and nRMS values between 1.0 and 2.3. In this case, results from ESK were significantly worse than results from Lei, probably due to the larger distance to the closest magnetic observatory.

Using SECS-ITF we were able to differentiate between local and regional signals (Figure 9). Figure 9a and 9b shows the contribution of the regional and local signals, respectively, at Lei and at ESK. Figure 9c shows the

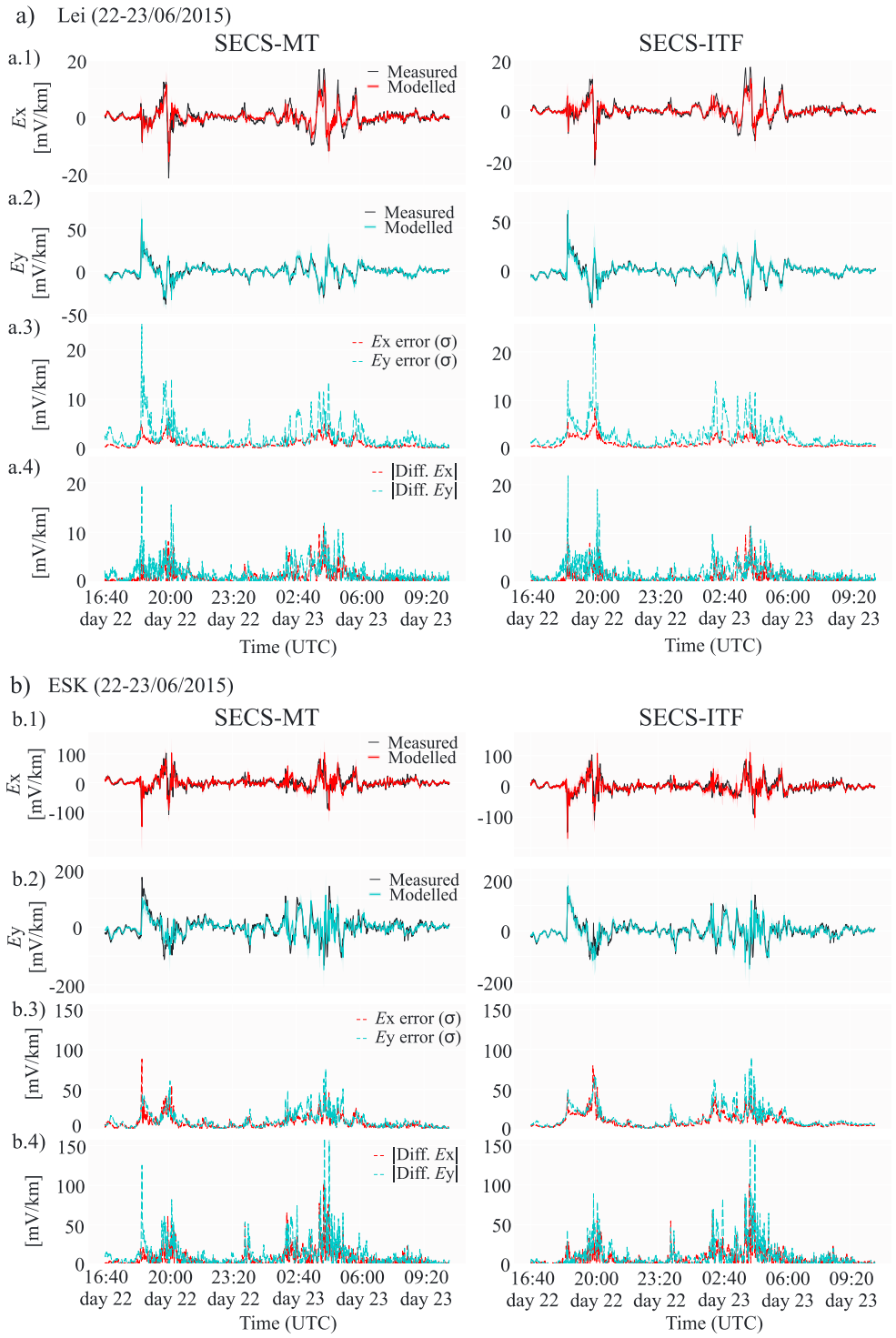

Figure 8. Modeled geoelectric fields at (a) Lei and (b) ESK during the geomagnetic storm in June 2015 following SECS-MT and SECS-ITF. (a1 and b1) The *x* (north-south) component of the geoelectric fields. Black is measured geoelectric fields and red modeled geoelectric fields. (a2 and b2) The *y* (east-west) components of the geoelectric fields. Black is measured geoelectric fields and blue modeled geoelectric fields. (a3 and b3) Estimated errors when computing geoelectric fields, red for *x* component and blue for *y* component. (a4 and b4) Differences between modeled and measured geoelectric fields. Red for *x* component and blue for *y* component.

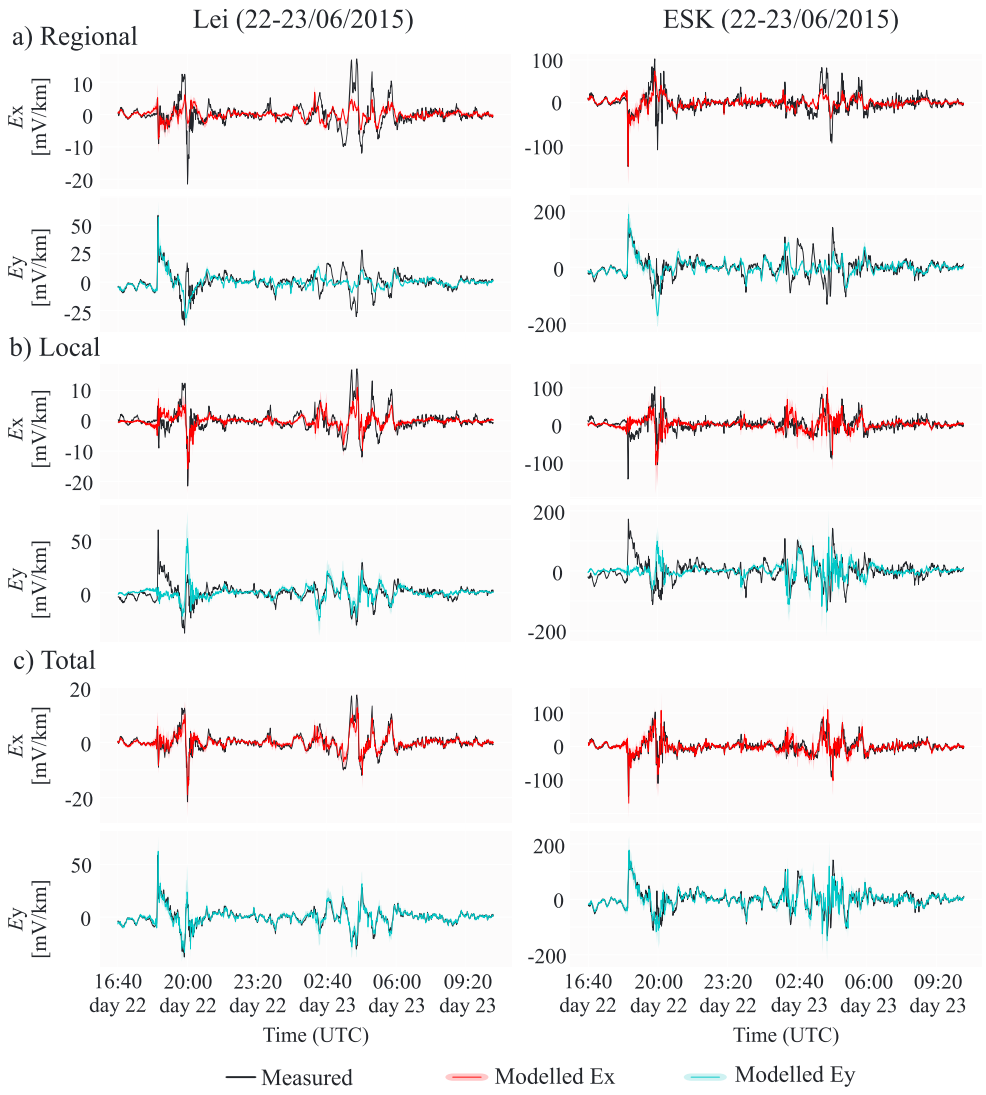

Figure 9. Modeled geoelectric fields at Lei and ESK during the geomagnetic storm in June 2015 following SECS-ITF. Red time series are the modeled *x* component of the geoelectric field and blue time series the modeled *y* component of the geoelectric field for (a) geoelectric field caused by the regional signal of the geomagnetic storm, (b) geoelectric field caused by the local signals of the geomagnetic storm, and (c) total geoelectric field. Black time series are the measured geoelectric field at Lei and ESK during the geomagnetic storm in June 2015. Lei = Leitrim; ESK = Eskdalemuir.

contribution of the total signal by adding the local and the regional contributions. Black time series represent the measured geoelectric fields at Lei and ESK. For this example and for these two sites, the sudden storm commencement at 18:33 on 22 June is dominated by regional sources, while the rest of the storm, including the main and the recovery phases, seems to be dominated by local sources.

4.2. Method Validation

SECS-MT and SECS-ITF were validated by modeling 34 geoelectric time series measured at Lei, HAD, and ESK during seven geomagnetic storms that occurred between 2013 and 2017: (1) 16–18 March 2013, (2) 24–26 May 2013, (3) 02–04 October 2013, (4) 11–13 September 2014, (5) 17–19 March 2015, (6) 27–29 May 2017, and (7) 07–09 September 2017. Results from the two approaches were compared with the measured time series, and with the results obtained when modeling the geoelectric fields using the magnetic field variations at the site of interest. Note that LER was not considered for the validation as it is located at the edge of the area of study and the interpolation of the magnetic field variations using SECS would not have been accurate. Figure 10 compares the accuracy of SECS-MT (blue) and SECS-ITF (orange) at modeling geoelectric fields with

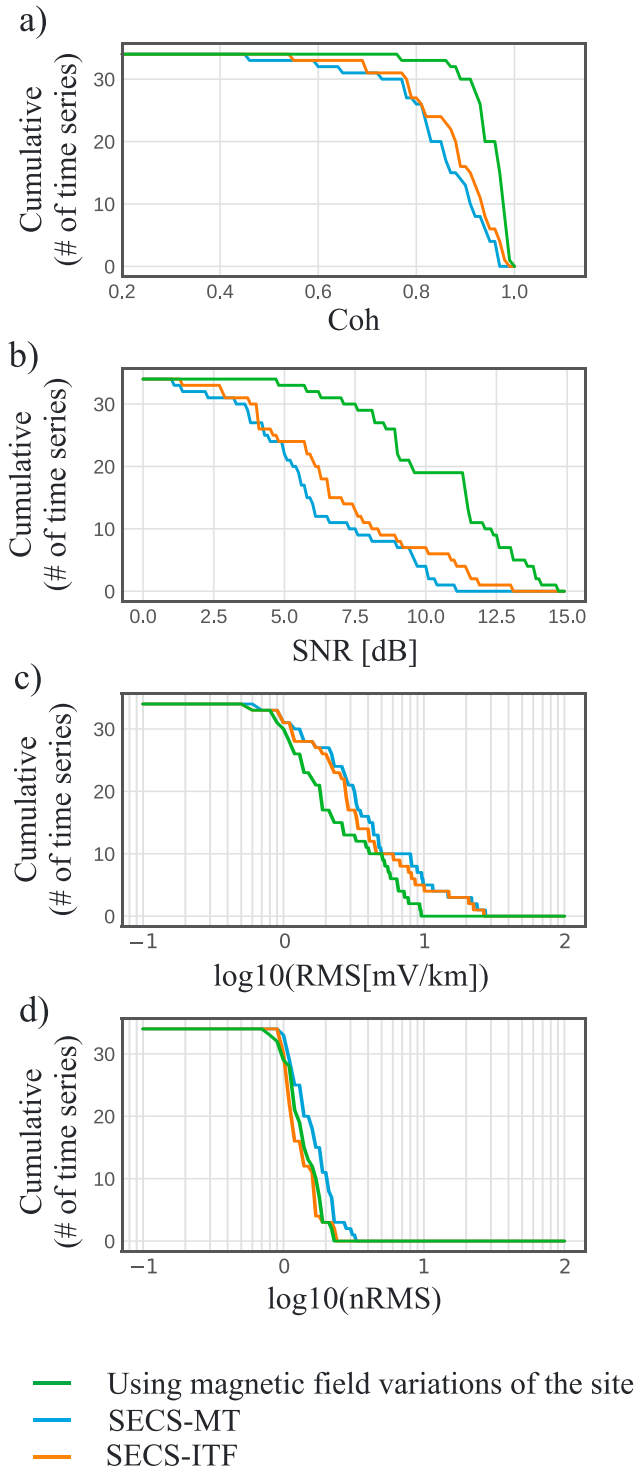

Figure 10. Evaluation of the accuracy at modeling 34 geoelectric time series at ESK, HAD, and Lei affected by several geomagnetic storms following three different approaches: Known magnetic field variations (green), SECS-MT (blue), and SECS-ITF (orange). The presented graphics show how many of the modeled geoelectric fields had (a) coherence, (b) SNR, (c) RMS, and (d) nRMS values larger than the values shown in the x-axis. Optimum values are (a) coherence values close to one, (b) large SNR values, (c) small RMS values, and (d) nRMS values close to one. SNR = signal-to-noise; RMS = eoot-mean-square; nRMS = normalized RMS.

the geoelectric fields generated using the magnetic field variations measured during the storms (green). The graphs show how many of the modeled geoelectric time series have Coh, SNR, RMS, and nRMS values larger than the values shown in the *x* axis. Figure 10 shows that knowing the magnetic field variations at the site of interest provides the best results. When this is not possible, SECS-ITF and SECS-MT approaches provide similar results but are consistently slightly better when using SECS-ITF. In addition, Figure 10d shows that nRMS values of SECS-ITF are closer to 1 than the nRMS values from SECS-MT, suggesting that the errors are better estimated using SECS-ITF. When modeling geoelectric fields using the SECS-ITF method the errors for local and regional sources were calculated separately and associated to different levels of accuracy, while using SECS-MT there was no differentiation between local and regional geomagnetic sources. Figure 6 previously showed better accuracy at interpolating the total rather than only the local geomagnetic fields, which concurs with the consideration that the errors associated with local and regional magnetic sources are different, and thus should be considered separately.

Figure 11 shows the accuracy of modeling geoelectric fields using Coh and SNR values in relation to the influence of local geomagnetic storms. The color of the data points is related to the distance of the site to the closest magnetic observatory. In general, the most obvious observation is that when the magnetic field variations at the site of interest are not known, there is a decrease in accuracy as the local effects became dominant. In relation to the distance to the closest magnetic observatory, no particular pattern is observed when the regional signal is dominant (values smaller than 0.5 on the *x* axis). However, when the local signal is dominant (values larger than 0.5 on the *x* axis) the dependence on the distance to the closest magnetic observatory is important and the accuracy reduces as the sites are located at larger distances from the closest magnetic observatory. The observed drop in accuracy for values between 0.4 and 0.5 on the *x* axis, in particular for the SNR, may be related to sources of noise affecting the measured geoelectric field. We argue this as most of these points are associated with the same site, HAD, where the drop was observed for all of the approaches used for modeling the geoelectric fields, including when the magnetic time series were known. Although is not easy to constrain the possible source of noise, a possible reason for the decrease in accuracy at HAD is its proximity to the coastline and the strong currents from the Bristol Channel, which can induce additional EM signals that cannot be reproduced using the plane wave method due to the proximity of the source. However, we also have to take into account that the measured electric and magnetic field variations were considered to be caused by geomagnetic activity, but sources of noise such as periodical cultural noise generated by human activity (i.e., power lines, electric fences, grounded pipelines, electric railways, and transformers), temperature effects, changes in the conductivity of the surface of the site where the electric fields were measured, or chemical reactions of the electrodes with the surrounding environment may also had affect the measured geoelectric fields. Segments of the time series significantly affected by noise (i.e., large steps) where not considered in the presented analysis.

5. Discussion

The results presented in this study show that we can achieve high accuracy when modeling geoelectric fields at a particular sites if the magnetic field

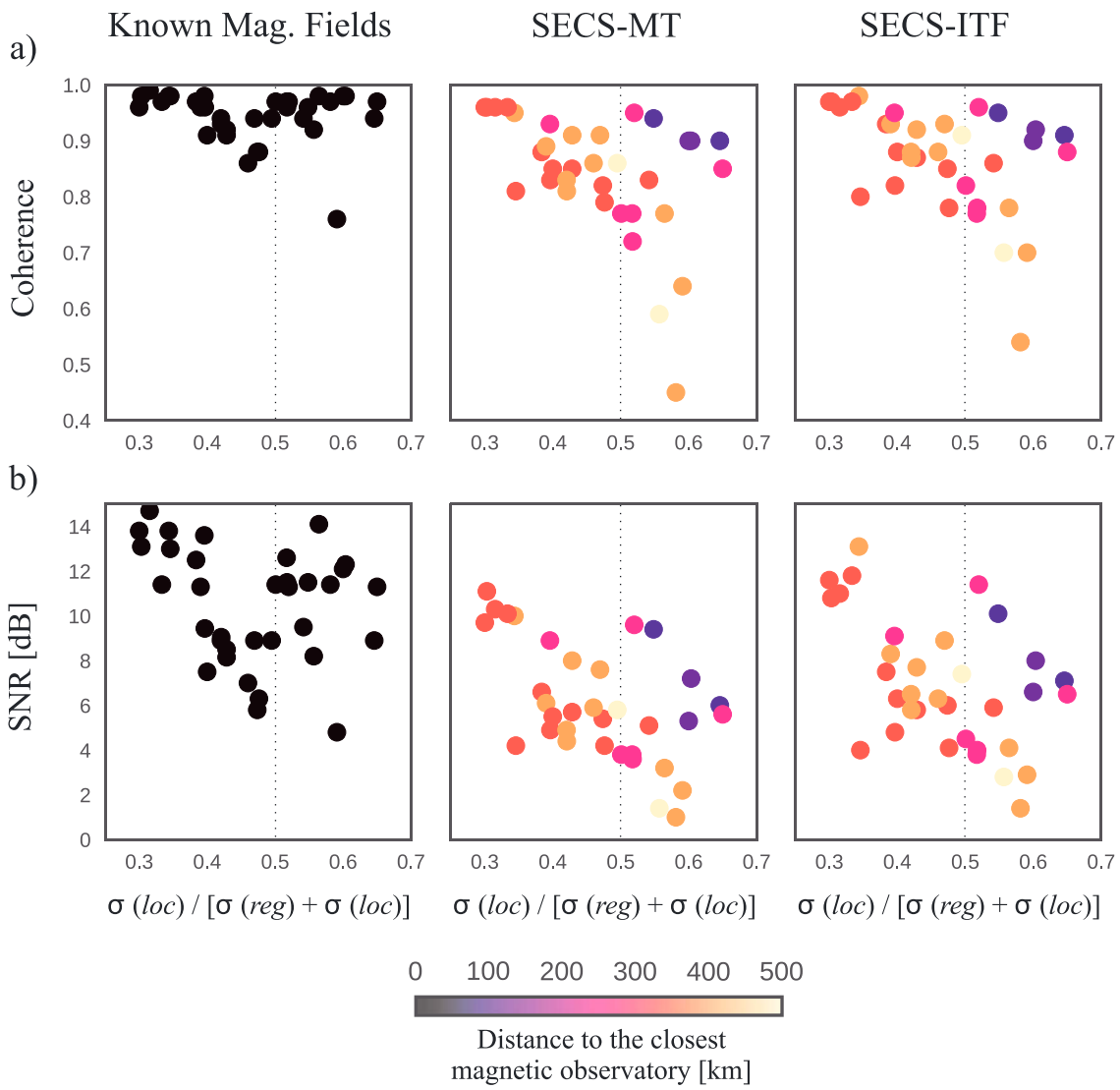

Figure 11. Accuracy at modeling geoelectric fields when the magnetic fields are known, using SECS-MT, and following SECS-ITF. (a) Coherence values when modeling geoelectric fields in relation to the influence of the local signal during the geomagnetic storms. (b) Signal-to-noise ratio (SNR) values at modeling geoelectric fields in relation to the influence of the local signal during the geomagnetic storms. Color indicate the distance to the closest magnetic observatory. Vertical dashed line shows when local and regional geomagnetic sources have similar intensity.

variations are known, and we recommend the SECS-ITF approach for modeling geoelectric fields at sites where no magnetic measurements were made during geomagnetic storms. The results also show that we can provide a reasonable estimation of the errors for the modeled geoelectric fields, constraining the uncertainties of the provided time series. With the present-day network of permanent magnetic observatories, we can expect Coh values between 0.5 and 0.99, in most of the cases larger than 0.75, and SNR values between 1 and 15 dB, in most of the cases above 4 dB when modeling the geoelectric fields in Ireland and the UK (Figure 10). Figure 11 shows that accuracy may decrease considerably for distances over above 100 km from the closest magnetic observatories when the geomagnetic storm is dominated by local effects. Equivalent results were observed by Butala et al. (2017) in the United States for three particular geomagnetic storms, showing that the accuracy at modeling GICs is strongly dependent on both magnetometer to substation transformers baseline distance and to the intensity of the geomagnetic storm, which can be associated with an increase of local effects. The largest distance to a magnetic observatory in Ireland is 200 km, while in the UK several areas are at more than 200 km from the closest magnetic observatory with the largest distance up to 400 km (Figure 1b). This issue could be solved by significantly increasing the

number of magnetic measurements. As local storms are associated with large variations of the magnetic field, low-resolution variometers, in comparison with the INTERMAGNET standards, could provide valuable data without implying large economic costs.

Another point of interest are the electrical properties of the subsurface geology. In Ireland and the UK the electrical resistivity values of the subsurface geology varies significantly over short distances, and several sites will be influenced by coastal effects. This means that a sparse spatial coverage of MT sites may result in lower accuracy results when modeling GICs. Although site location based on geology and known tectonic terranes will optimize the number of necessary MT measurements, similar tensor relationships between nearby sites will indicate a good coverage of sites, while large differences between nearby sites will suggest the need of higher density of stations in this particular region. The use of long period magnetotelluric data already acquired in Ireland (Rao et al., 2014), and the outputs from projects currently under development such as SWEMDI, funded by the Geological Survey of Ireland, and SWIGS, funded by the Natural Environment Research Council, will provide new tensor relationships over Ireland and the UK increasing the spatial resolution when constraining the Earth response to magnetic field variations.

In relation to the study of GICs, the direct use of the full tensor relationships, considering 3-D effects of the subsurface geology, has shown to be valuable for modeling GICs. Torta et al. (2017) demonstrated that the MT impedance tensor can properly represent the response of the regional geological structures. Their results showed that local surveys can provide a practical solution for power grid nodes identified as being at risk from GICs when the electric field over the area containing the whole length of the power lines feeding into the at-risk nodes is suitably constrained. Recent results from Lucas et al. (2018) also suggest the use of the full tensor relationship as an appropriate approach for constraining the geoelectric fields used to model the GICs. The presented approaches in this manuscript, in particular SECS-ITF, will allow us to improve prior assessments of GIC risk, thus enabling operators to assess risks in advance and to be ready to deal with those risks. It will also provide valuable data for postevent analysis if anomalies detected are due to GICs.

The presented approaches also provide the possibility of creating a large database of geoelectric fields time series using several years of magnetic time series from the magnetic observatories. This data set can be used to train, test, and validate new approaches for now-casting and forecasting either geoelectric field time series or geoelectric field conditions using, for example, magnetic data from the magnetic observatories or satellite data from Lagrangian L1 point. Further studies in this direction will evaluate the applicability and accuracy for now-casting and forecasting geoelectric fields in Ireland and the UK, and the expected levels of accuracy. In the case of success, this will provide valuable data for operators being able to monitor if any problems they observe are directly related to geomagnetic activity (and not to other issues) and allow the implementation of measures for mitigating against the effects of solar storms.

6. Conclusions

This study evaluated the possibilities for modeling geoelectric fields caused by geomagnetic storms in Ireland and the UK using two approaches, SECS-MT and SECS-ITF, showing that we can accurately reproduce the geoelectric fields during quiet time and storm time. The presented approaches, in particular SECS-ITF, can provide better prior assessments and more detailed analysis of GIC risks, not only by providing more accurate results when modeling geoelectric fields but also by including an error estimation, and by being able to differentiate between the effects of local and regional geomagnetic sources. SECS-MT and SECS-ITF can also be used to create a reliable database of geoelectric field time series at sites where measurements were performed only for a short interval of time, which can be used to test now-casting and forecasting approaches.

The prior analysis performed before modeling geoelectric fields showed that (1) although most of the analyzed periods are affected by geomagnetic storms, ~90% of the var signal, related to magnetic field variations caused by geomagnetic storms, can be explained using periods between 30 and 30,000 s. If periods between 120 and 20,000 s are used, as in this study, ~78% of the var signal can be explained, (2) the electrical properties of the subsurface geology has an important role at defining the electric but also the magnetic field variations measured at the Earth's surface, and (3) at least three types of errors should be considered when modeling geoelectric fields including errors associate with (i) errors from the tensor relationships, (ii) the

assumption of the plane wave approximation, and (iii) the accuracy of interpolating magnetic field variations using SECS.

The expected levels of accuracy at modeling geoelectric fields using SECS-ITF are (1) coherence values between 0.5 and 0.95, in most of the cases above 0.75 and (2) SNR values between 1 and 15 dB, in most of the cases above 4 dB. The expected resolution within these ranges of values may depend on the influence of the local geomagnetic sources during a geomagnetic storm, and on the distance of the site of interest to the closest magnetic observatory. Sites in close proximity ($<$100 km) to a magnetic observatory and affected by a geomagnetic storm dominated by regional signal will provide the most accurate results, while sites located at further distances from the geomagnetic observatories and affected by a geomagnetic storm dominated by local effects will be less accurate.

New magnetic measurements at a higher spatial resolution, and new electromagnetic transfer functions constraining the Earth's response to magnetic field variations would provide major improvements for modeling and understanding the geoelectric fields in Ireland and the UK and increase the accuracy when modeling GICs and evaluating mitigation strategies.

Acknowledgments

This research is supported by the Irish Research Council's Enterprise Partnership Scheme between Trinity College Dublin and Met Office (EPSPD/2016/22). We thank the Irish Research Council and Met Office for support for Joan Campanyà and the Irish Research Council and Eirgrid plc for support for Seán Blake. Ciarán D. Beggan, and Gemma S. Richardson were supported by Natural Environment Research Council grant NE/P017231/1 *Space Weather Impacts on Ground-based Systems431 (SWIGS)*. This research has benefited from a Royal Society/Royal Irish Academy International Exchange grant (IE150685). We would like to acknowledge that the results presented in this paper rely on data collected at magnetic observatories. We thank the national institutes that support the magnetic observatories and INTERMAGNET for promoting high standards of magnetic observatory practice (www.intermagnet.org). We also acknowledge Armagh Observatory for hosting a magnetometer that contributed to this work. Data from magnetic observatories are available from INTERMAGNET (www.intermagnet.org) and the Rosse observatory (http://www.rosseobservatory.ie/data). Electric time series from HAD, ESK, and LER are available from the British Geological Survey (BGS, http://www.geomag.bgs.ac.uk/data_service/space_weather/geoelectric.html). The algorithms presented in this paper, SECS-ITF and SECS-MT, with data from the examples presented in this manuscript, are available in Github (https://github.com/joancampanya/Compute_GeoElectric_Fields).

References

Albertson, V. D., & Thorson, J. M. (1974). Power system disturbances during a K-8 geomagnetic storm: August 4, 1972. *IEEE Transactions on Power Apparatus and Systems*, *PAS-93*(4), 1025–1030. https://doi.org/10.1109/TPAS.1974.294046

Allen, J., Sauer, H., Frank, L., & Reiff, P. (1989). Effects of the March 1989 solar activity. *Eos, Transactions American Geophysical Union*, *70*(46), 1479. https://doi.org/10.1029/89EO00409

Amm, O., & Viljanen, A. (1999). Ionospheric disturbance magnetic field continuation from the ground to the ionosphere using spherical elementary current systems. *Earth, Planets and Space*, *51*(6), 431–440. https://www.terrapub.co.jp/journals/EPS/pdf/5106/51060431.pdf

Bailey, R. L., Halbedl, T. S., Schattauer, I., Römer, A., Achleitner, G., Beggan, C. D., et al. (2017). Modelling geomagnetically induced currents in midlatitude Central Europe using a thin-sheet approach. *Annales de Geophysique*, *35*(3), 751–761. https://doi.org/10.5194/angeo-35-751-2017

Barbosa, C., Alves, L., Caraballo, R., Hartmann, G. A., Papa, A. R. R., & Pirjola, R. J. (2015). Analysis of Geomagnetically induced currents at a low-latitude region over the solar cycles 23 and 24: Comparison between measurements and calculations. *Journal of Space Weather and Space Climate*, *5*, A35. https://doi.org/10.1051/swsc/2015036

Bedrosian, P. A., & Love, J. J. (2015). Mapping geoelectric fields during magnetic storms: Synthetic analysis of empirical United States impedances. *Geophysical Research Letters*, *42*, 10,160–10,170. https://doi.org/10.1002/2015GL066636

Beggan, C. D., Beamish, D., Richards, A., Kelly, G. S., & Thomson, A. W. P. (2013). Prediction of extreme geomagnetically induced currents in the UK high-voltage network. *Space Weather*, *11*, 407–419. https://doi.org/10.1002/swe.20065

Béland, J., & Small, K. (2004). Space weather effects on power transmission systems: The cases of Hydro-Québec and transpower New Zealand Ltd. In *Effects of space weather on technology infrastructure* (pp. 287–299). Dordrecht: Kluwer Academic Publishers. https://doi.org/10.1007/1-4020-2754-0_15

Berdichevsky, M. N., & Dmitriev, V. I. (2008). *Models and methods of magnetotellurics*. Springer. Retrieved from https://books.google.ie/books?id=-Fs8cPqeCcQC&pg=PA4&lpg=PA4&dq=Berdichevsky+and+dimitriev&source=bl&ots=2CaMxmL08v&sig=YvJ--LgFPQip0ztNAMQAuN5l1KY&hl=ca&sa=X&ved=0ahUKEwijlcj5yebXAhWLKVAKHUwvAWwQ6AEINzAF#v=onepage&q=Berdichevsky and dimitriev&f=false

Blake, B., Seán, P., Gallagher, P. T., Campanyà, J., Hogg, C., Beggan, C. D., et al. (2018). A detailed model of the Irish high voltage power network for simulating GICs. *Space Weather*, *16*, 1770–1783. https://doi.org/10.1029/2018SW001926

Blake, S. P., Gallagher, P. T., McCauley, J., Jones, A. G., Hogg, C., Campanyà, J., et al. (2016). Geomagnetically induced currents in the Irish power network during geomagnetic storms. *Space Weather*, *14*, 1136–1154. https://doi.org/10.1002/2016SW001534

Bolduc, L. (2002). GIC observations and studies in the Hydro-Québec power system. *Journal of Atmospheric and Solar-Terrestrial Physics*, *64*(16), 1793–1802. https://doi.org/10.1016/S1364-6826(02)00128-1

Bonner, L. R., & Schultz, A. (2017). Rapid prediction of electric fields associated with geomagnetically induced currents in the presence of three-dimensional ground structure: Projection of remote magnetic observatory data through magnetotelluric impedance tensors. *Space Weather*, *15*, 204–227. https://doi.org/10.1002/2016SW001535

Boteler, D. H., & Pirjola, R. J. (1998). The complex-image method for calculating the magnetic and electric fields produced at the surface of the Earth by the auroral electrojet. *Geophysical Journal International*, *132*(1), 31–40.

Boteler, D. H., & Pirjola, R. J. (2017). Modeling geomagnetically induced currents. *Space Weather*, *15*, 258–276. https://doi.org/10.1002/2016SW001499

Butala, M. D., Kazerooni, M., Makela, J. J., Kamalabadi, F., Gannon, J. L., Zhu, H., & Overbye, T. J. (2017). Modeling geomagnetically induced currents from magnetometer measurements: Spatial scale assessed with reference measurements. *Space Weather*, *15*, 1357–1372. https://doi.org/10.1002/2017SW001602

Campanya, J., Ledo, J., Queralt, P., Marcuello, A., & Jones, A. G. (2014). A new methodology to estimate magnetotelluric (MT) tensor relationships: Estimation of Local Transfer-Functions by Combining Interstation Transfer-Functions (ELICIT). *Geophysical Journal International*, *198*(1), 484–494. https://doi.org/10.1093/gji/ggu147

Chave, A. D., & Jones, A. G. (2012). *The Magnetotelluric Method*. Cambridge: Cambridge University Press. https://doi.org/10.1017/CBO9781139020138

Chave, A. D., & Thomson, D. J. (2004). Bounded influence magnetotelluric response function estimation. *Geophysical Journal International*, *157*(3), 988–1006. https://doi.org/10.1111/j.1365-246X.2004.02203.x

Cliver, E. W., & Dietrich, W. F. (2013). The 1859 space weather event revisited: Limits of extreme activity. *Journal of Space Weather and Space Climate*, *3* EDP Sciences, A31. https://doi.org/10.1051/swsc/2013053

Eastwood, J. P., Biffis, E., Hapgood, M. A., Green, L., Bisi, M. M., Bentley, R. D., et al. (2017). The economic impact of space weather: Where do we stand? *Risk Analysis*, *37*(2), 206–218. https://doi.org/10.1111/risa.12765

Gamble, T. D., Goubau, W. M., & Clarke, J. (1979a). Magnetotellurics with a remote magnetic reference. *Geophysics*, *44*(1), 53–68. https://doi.org/10.1190/1.1440923

Gamble, T. D., Goubau, W. M., & Clarke, J. (1979b). Error analysis for remote reference magnetotellurics. *Geophysics*, *44*(5), 959–968. https://doi.org/10.1190/1.1440988

García, X., & Jones, A. G. (2005). A new methodology for the acquisition and processing of audio-magnetotelluric (AMT) data in the AMT dead band. *Geophysics*, *70*(5), G119–G126. https://doi.org/10.1190/1.2073889

Gaunt, C. T., & Coetzee, G. (2007). Transformer failures in regions incorrectly considered to have low GIC-Risk. In *2007 IEEE Lausanne Power Tech* (pp. 807–812). Lausanne, Switzerland: IEEE. https://doi.org/10.1109/PCT.2007.4538419

Ivannikova, E., Kruglyakov, M., Kuvshinov, A., Rastätter, L., & Pulkkinen, A. (2018). Regional 3-D modeling of ground electromagnetic field due to eealistic geomagnetic disturbances. *Space Weather*, *16*, 476–500. https://doi.org/10.1002/2017SW001793

Johnsen, M. G. (2013). Real-time determination and monitoring of the auroral electrojet boundaries. *Journal of Space Weather and Space Climate*, *3*. EDP Sciences, A28. https://doi.org/10.1051/swsc/2013050

Jones, A. G., & Hutton, V. R. S. (1979). A multi-station magnetotelluric study in southern Scotland 1. Field work, data analysis and results. *Geophysical Journal of the Royal Astronomical Society*, *56*, 329–349.

Kappenman, J. G. (2005). An overview of the impulsive geomagnetic field disturbances and power grid impacts associated with the violent Sun-earth connection events of 29–31 October 2003 and a comparative evaluation with other contemporary storms. *Space Weather*, *3*, S08C01. https://doi.org/10.1029/2004SW000128

Kataoka, R., & Iwahashi, K. (2017). Inclined zenith Aurora over Kyoto on 17 September 1770: Graphical evidence of extreme magnetic storm. *Space Weather*, *15*, 1314–1320. https://doi.org/10.1002/2017SW001690

Kelbert, A., Balch, C. C., Pulkkinen, A., Egbert, G. D., Love, J. J., Joshua Rigler, E., & Fujii, I. (2017). Methodology for time-domain estimation of storm-time geoelectric fields using the 3D magnetotelluric response tensors. *Space Weather* https://doi.org/10.1002/2017SW001594, *15*, 874–894.

Kelly, G. S., Viljanen, A., Beggan, C. D., & Thomson, A. W. P. (2017). Understanding GIC in the UK and French high-voltage transmission systems during severe magnetic storms. *Space Weather*, *15*, 99–114. https://doi.org/10.1002/2016SW001469

Koen, J., & Gaunt, T. (2003). Geomagnetically Induced Currents in the Southern African Electricity Transmission Network, IEEE Bologna PowerTech Conference. https://doi.org/10.1109/PTC.2003.1304165

Lucas, G. M., Love, J. J., & Kelbert, A. (2018). Calculation of voltages in electric power transmission lines during historic geomagnetic storms: An investigation using realistic earth impedances. *Space Weather*, *16*, 185–195. https://doi.org/10.1002/2017SW001779

McLay, S. A., & Beggan, C. D. (2011). Interpolation of externally-caused magnetic fields over large sparse arrays using Spherical Elementary Current Systems. *Annales Geophysicae*, *28*, 1795–1805.

Marshall, R. A., Dalzell, M., Waters, C. L., Goldthorpe, P., & Smith, E. A. (2012). Geomagnetically induced currents in the New Zealand power network. *Space Weather*, *10*, S08003. https://doi.org/10.1029/2012SW000806

Ngwira, C. M., McKinnell, L.-A., & Cilliers, P. J. (2011). Geomagnetic activity indicators for geomagnetically induced current studies in South Africa. *Advances in Space Research*, *48*(3), 529–534. https://doi.org/10.1016/j.asr.2011.03.042

Oughton, E. J., Skelton, A., Horne, R. B., Thomson, A. W. P., & Gaunt, C. T. (2017). Quantifying the daily economic impact of extreme space weather due to failure in electricity transmission infrastructure. *Space Weather*, *15*, 65–83. https://doi.org/10.1002/2016SW001491

Pirjola, R. (2000). Geomagnetically induced currents during magnetic storms. *IEEE Transactions on Plasma Science*, *28*(6), 1867–1873. https://doi.org/10.1109/27.902215

Pulkkinen, A., Bernabeu, E., Thomson, A., Viljanen, A., Pirjola, R., Boteler, D., et al. (2017). Geomagnetically induced currents: science, engineering, and applications readiness. *Space Weather*, *15*, 828–856. https://doi.org/10.1002/2016SW001501

Rao, C. K., Jones, A. G., & Moorkamp, M. (2007). The geometry of the Iapetus suture zone in central Ireland deduced from a magnetotelluric study. *Physics of the Earth and Planetary Interiors*, *161*, 134–141.

Rao, C. K., Jones, A. G., Moorkamp, M., & Weckmann, U. (2014). Implications for the lithospheric geometry of the Iapetus suture beneath Ireland based on electrical resistivity models from deep-probing magnetotellurics. *Geophysical Journal International*, *198*, 737–759.

Romano, G., Balasco, M., Lapenna, V., Siniscalchi, A., Telesca, L., & Tripaldi, S. (2014). On the sensitivity of long-term magnetotelluric monitoring in Southern Italy and source-dependent robust single station transfer function variability. *Geophysical Journal International*, *197*(3), 1425–1441.

Rostoker, G. (1972). Geomagnetic indices. *Reviews of Gephysics*, *10*(4), 935–950. https://doi.org/10.1029/RG010i004p00935

Sule, P. O., Hutton, V. R. S., & Dumitrescu, C. (1993). Subsurface structure of SE Scotland from broad-band magnetotelluric measurements. *Physics of the Earth and Planetary Interiors*, *81*, 91–24.

Torta, J. M., Marcuello, A., Campanyà, J., Marsal, S., Queralt, P., & Ledo, J. (2017). Improving the modeling of geomagnetically induced currents in Spain. *Space Weather*, *15*, 691–703. https://doi.org/10.1002/2017SW001628

Torta, J., Marsal, S., & Quintana, M. (2014). Assessing the Hazard from Geomagnetically induced currents to the entire high-voltage power network in Spain. *Earth, Planets and Space*, *66*(1), 87. https://doi.org/10.1186/1880-5981-66-87

Varentsov, I. M., Sokolova, E. Y., & Bear, W. G. (2003). Diagnostics and suppression of auroral distortions in the transfer operators of the EM field in the BEAR experiment. *Izvestiya, Physics of the Solid Earth*, *39*(4), 283–307.

Wang, H., Campanyà, J., Cheng, J., Zhu, G., Wei, W., Jin, S., & Ye, G. (2017). Synthesis of natural electric and magnetic time-series using interstation transfer functions and time-series from a neighboring site (STIN): Applications for processing MT data. *Journal of Geophysical Research: Solid Earth*, *122*, 5835–5851. https://doi.org/10.1002/2017JB014190

Weigel, R. S. (2017). "A comparison of methods for estimating the geoelectric field." *Space Weather*, *15*, 430–440. https://doi.org/10.1002/2016SW001504

Zhang, J. J., Wang, C., Sun, T. R., Liu, C. M., & Wang, K. R. (2015). GIC due to storm sudden commencement in low-latitude high-voltage power network in China: Observation and simulation. *Space Weather*, *13*, 643–655. https://doi.org/10.1002/2015SW001263